

Galactic spiral patterns and dynamo action I: A new twist on magnetic arms

Luke Chamandy¹, Kandaswamy Subramanian¹ & Anvar Shukurov^{2,1} *

¹Inter-University Centre for Astronomy and Astrophysics, Post Bag 4, Ganeshkhind, Pune 411007, India

²School of Mathematics & Statistics, Newcastle University, Newcastle upon Tyne NE1 7RU

Submitted to MNRAS

ABSTRACT

We generalise the theory of mean-field galactic dynamos by allowing for temporal non-locality in the mean electromotive force (emf). This arises in random flows due to a finite response time of the mean emf to changes in the mean magnetic field, and leads to the telegraph equation for the mean field. The resulting dynamo model also includes the nonlinear dynamo effects arising from magnetic helicity balance. Within this framework, coherent large-scale magnetic spiral arms superimposed on the dominant axially symmetric magnetic structure are considered. A non-axisymmetric forcing of the mean-field dynamo by a spiral pattern (either stationary or transient) is invoked, with the aim of explaining the phenomenon of magnetic arms. For a stationary dynamo forcing by a rigidly rotating material spiral, we find corotating non-axisymmetric magnetic modes enslaved to the axisymmetric modes and strongly peaked around the corotation radius. For a forcing by transient material arms wound up by the galactic differential rotation, the magnetic spiral is able to adjust to the winding so that it resembles the material spiral at all times. There are profound effects associated with the temporal non-locality, i.e. finite ‘dynamo relaxation time’. For the case of a rigidly rotating spiral, a finite relaxation time causes each magnetic arm to mostly lag the corresponding material arm with respect to the rotation. For a transient material spiral that winds up, the finite dynamo relaxation time leads to a large, negative (in the sense of the rotation) phase shift between the magnetic and material arms, similar to that observed in NGC 6946 and other galaxies. We confirm that sufficiently strong random seed fields can lead to global reversals of the regular field along the radius whose long-term survival depend on specific features of a given galaxy.

Key words: magnetic fields – MHD – galaxies: magnetic fields – galaxies: spiral – galaxies: structure

1 INTRODUCTION

Nearby disc galaxies are known to typically have regular (or large-scale or mean) magnetic fields of $1\text{--}10\,\mu\text{G}$ in strength, which are coherent on the scale of the galaxies themselves (see Fletcher 2010; Beck 2012, for reviews). In many cases, galactic magnetic fields exhibit significant deviations from axial symmetry, in particular where the regular field is enhanced in ‘spiral magnetic arms’ akin to the material arms. (By material arms, we specifically mean the regions where the densities of stars and gas are enhanced.) In most cases, there is clearly a relationship between the material spiral arms and regular magnetic field spiral arms. For instance, there exists a correspondence between the azimuthally av-

eraged pitch angle of the regular field and that of the material spiral (Fletcher 2010). This would be of little surprise, as the material arms naturally leave their imprint on the magnetic field, if not for the intriguing relation between magnetic and material arms, first discovered in the nearby galaxy NGC 6946 (Beck & Hoernes 1996). Here the magnetic arms are located almost precisely between the material arms. They appear to be phase-shifted images of the material arms, with a negative phase shift in the sense of the galactic rotation (Frick et al. 2000; Beck 2007). Importantly, the stronger tangling of the regular field by a (presumably) more intense turbulence within the material arms cannot explain this phenomenon: both the total and regular magnetic fields are stronger within the magnetic arms (Beck 2007). The nature of magnetic arms remains to be convincingly explained.

* E-mail: lchamandy@gmail.com (LC); kandu@iucaa.ernet.in (KS); anvar.shukurov@newcastle.ac.uk (AS)

1.1 Magnetic arms and dynamo theory

Turbulent mean-field dynamo theory has been successful in explaining the properties of the axisymmetric mode of regular fields in galaxies (Ruzmaikin et al. 1988, hereafter RSS88).

Although growing non-axisymmetric modes can arise in this theory (beyond a certain radius in the disc where the rotational velocity shear is sufficiently small), they always have a lower growth rate than the axisymmetric mode if the galactic disc is axially symmetric (Baryshnikova et al. 1987; Krasheninnikova et al. 1989). Thus, to explain non-axisymmetric modes as arising in an axisymmetric disc one must typically appeal to strongly non-axisymmetric seed fields and argue that the axisymmetric mode would not have had time to attain dominance. As we argue in this work, incorporating field saturation through nonlinear feedback does not help the non-axisymmetric modes to become entrenched in an axisymmetric disc, and in fact causes them to eventually decay.

An alternative, of course, is to appeal to the deviations of the galactic discs from axial symmetry. Mestel & Subramanian (1991, hereafter MS91) and Subramanian & Mestel (1993, hereafter SM93) explored analytically and numerically the growth of non-axisymmetric modes under an enhancement of dynamo action along a spiral (presumably, but not necessarily, co-spatial with the material spiral) with a constant global pattern speed. Subsequently, Moss (1996, hereafter M96) (see also Moss 1998; Moss et al. 2001) carried out mean-field dynamo simulations to explore the effects of modulating various quantities, such as the α effect, turbulent diffusivity, or the components of the mean velocity, along a spiral arm or bar. Some authors have also addressed directly the question of how the regular field could become enhanced in between the material arms (Shukurov 2005; Rohde et al. 1999), though none of these explained the phenomenon of a substantial negative phase shift across a wide range of galactocentric distances, including those far away from the corotation radius, as reported by Frick et al. (2000).

The earlier attempts to explain the phenomenon of magnetic arms encountered a fundamental difficulty of the same nature as in theory of spiral structure: it is feasible to maintain a significant phase difference between material and magnetic arms near the corotation radius, but the differential rotation of the galaxy quickly winds up the magnetic arms to destroy the arms away from the corotation. In other words, in order to explain a constant phase shift between magnetic and material spiral arms, the former have to rotate rigidly. There are two important implications. Firstly, the large-scale magnetic field in magnetic arms cannot be frozen into the interstellar gas. Secondly, the governing equations for the large-scale magnetic field must have wave-like solutions. The former implication is fully consistent with the mean-field dynamo theory where turbulent magnetic diffusivity can ensure the slippage of the large-scale magnetic field at appropriate time scales. However, the latter feature requires a significant extension of the existing theory since the leading growing modes of the standard mean-field dynamo equations in a thin disc are non-oscillatory (in contrast to spherical geometry, where dynamo waves can occur). Thus, any attempt to explain magnetic arms within

the framework of mean-field dynamos requires a substantial generalization of the theory. One such generalization is proposed here.

1.2 Advances in dynamo and spiral structure theories

Much of the recent work on mean-field dynamo theory has been focussed on the nonlinear regime, and the possible catastrophic quenching of the dynamo implied by magnetic helicity conservation. This has led to the development of the dynamical quenching theory (see the review of Brandenburg & Subramanian 2005a, hereafter BS05). In this theory, catastrophic quenching of the mean-field dynamo action is averted by a magnetic helicity flux, which transports small-scale magnetic helicity away from the region of dynamo action. Dynamical quenching theory has been applied to local galactic dynamo models (Kleeorin et al. 2000; Vishniac & Cho 2001; Kleeorin et al. 2002; Shukurov et al. 2006; Sur et al. 2007), and to axisymmetric discs (Kleeorin et al. 2002; Smith 2012; Smith et al. 2012), but not yet to non-axisymmetric mean-field disc dynamos. Past work on the non-axisymmetric disc dynamos focused on the linear (kinematic) regime, or relied on an approximate algebraic quenching formalism.

Another recent development is the emergence of the minimal- τ approximation (MTA) as a more general closure for mean-field electrodynamics that includes the quasilinear or first-order smoothing approximation (FOSA) as a limiting case (Kleeorin et al. 1996; Rogachevskii & Kleeorin 2000; Blackman & Field 2002; BS05). MTA is physically more appealing than FOSA because it takes into account the finite response time of the mean electromotive force (emf) to changes in the mean magnetic field. This closure leads to new terms in the mean induction equation, which becomes a telegraph-type equation (Courant & Hilbert 1989), with second-order time derivative of the mean magnetic field. Separate considerations, motivated in part by the need to incorporate the non-locality in the dynamo coefficients, lead to essentially the same telegraph-type equation (Rheinhardt & Brandenburg 2012, see also Hughes & Proctor 2010). Such non-locality in time could lead to important effects in disc galaxies, where the product of the gas angular velocity ω and correlation time of the turbulence τ_c may be of the order unity. Most notably, we find that it may lead to a large negative phase shift (in the sense of the galactic rotation) between the magnetic spiral arms and material spiral arms. For instance, for a spiral pattern rotating with pattern speed Ω , one might expect a phase shift of order $\Omega\tau_c$, due to the delay of order τ_c in the response of the mean emf to the enhanced α effect in the spiral arms.

Yet another significant development has been the emergence of strong evidence that spiral patterns are not, at least in some cases, long-lived features rotating at a single constant pattern speed (Shetty et al. 2007; Dobbs et al. 2010; Sellwood 2011; Quillen et al. 2011; Roškar et al. 2011; Wada et al. 2011; Dobbs 2011; Kawata et al. 2011; Khoperskov et al. 2011). Theory, observations, and especially simulations of isolated and interacting galaxies point to a wide spectrum of possibilities, from relatively rigidly-rotating and long-lived patterns with fairly constant pattern speeds, to composite spirals comprised of multiple pattern speeds dom-

inating in different radial ranges, to material arms that appear to rotate with the local gas velocity and thus quickly wind up.

The goal of the present work is to draw together these recent developments in dynamo theory and spiral structure and apply the new ideas to examine non-axisymmetric regular magnetic fields in disc galaxies. Here we focus on modes that are enslaved to the axisymmetric mode (and thus have the same growth rate in the kinematic regime); for a two-armed material spiral this would mean the quadrupole mode (or $m = 2$ mode of the Fourier expansion) that corotates with the spiral pattern, as well as other even- m corotating modes, which are weaker. Here we discuss a numerical model, while Chamandy et al. (2012b, hereafter Paper II) presents a semi-analytical treatment of such modes. We leave the bisymmetric ($m = 1$) mode and other odd- m corotating modes to a forthcoming paper. Where the present work differs importantly from previous work is that here we:

- (i) incorporate MTA and explore the effects of a finite dynamo relaxation time;
- (ii) include dynamical quenching with an advective helicity flux for non-axisymmetric modes; and
- (iii) explore the effects of both rigidly rotating and transient material arms on the mean magnetic field.

In addition to this work on non-axisymmetric mean-field dynamos, we also briefly report on some new results from mean-field dynamo simulations which use an axisymmetric disc.

The plan of the paper is as follows. We present in Section 2 the basic equations and introduce our mathematical approach. We outline the numerical model in Section 3. In Sect. 4 we discuss the findings from simulations of axisymmetric discs, while in Sections 5 and 6 we describe the results of simulations of non-axisymmetric discs. A discussion of results and our conclusions are presented in Section 7.

2 THE MEAN-FIELD DYNAMO AND THE TELEGRAPH EQUATION

Consider the induction equation given by

$$\frac{\partial \mathbf{B}}{\partial t} = \nabla \times (\mathbf{U} \times \mathbf{B} - \eta \nabla \times \mathbf{B}), \quad (1)$$

where \mathbf{B} is the magnetic field, \mathbf{U} is the velocity field, η is the magnetic diffusivity. We follow the mean-field approach where the velocity and magnetic fields are each written as the sum of an average and a random component,

$$\mathbf{B} = \overline{\mathbf{B}} + \mathbf{b} \quad \text{and} \quad \mathbf{U} = \overline{\mathbf{U}} + \mathbf{u}. \quad (2)$$

Here bar formally represents ensemble averaging but for practical purposes can be thought of as spatial average over scales larger than the turbulent scale but smaller than the system size. Substituting Eq. (2) into the induction equation leads to the mean-field induction equation (Moffatt 1978; Krause & Raedler 1980),

$$\frac{\partial \overline{\mathbf{B}}}{\partial t} = \nabla \times (\overline{\mathbf{U}} \times \overline{\mathbf{B}} + \mathcal{E} - \eta \nabla \times \overline{\mathbf{B}}). \quad (3)$$

where

$$\mathcal{E} = \overline{\mathbf{u} \cdot \nabla \times \mathbf{b}} \quad (4)$$

is the mean electromotive force.

Expressing \mathcal{E} in terms of the mean field is a standard closure problem. A relatively simple and widely used closure is the quasilinear approximation, also known as the first-order smoothing approximation (FOSA; Moffatt 1978; Krause & Raedler 1980; BS05). In the quasilinear theory or FOSA, one neglects nonlinear terms in the evolution equation for \mathbf{u} and \mathbf{b} , which, however, are retained if an evolution equation for \mathcal{E} is used instead (see below). For isotropic, helical turbulence, it leads to an expansion whose lowest-order terms are given by

$$\mathcal{E} = \alpha \overline{\mathbf{B}} - \eta_t \nabla \times \overline{\mathbf{B}}, \quad (5)$$

where, in the kinematic limit, $\alpha = \alpha_k$ with

$$\alpha_k = -\frac{1}{3} \tau_c \overline{\mathbf{u} \cdot \nabla \times \mathbf{u}}, \quad \eta_t = \frac{1}{3} \tau_c \overline{\mathbf{u}^2}, \quad (6)$$

and τ_c is the correlation time of the random flow. The turbulent transport coefficients α and η_t are proportional, respectively, to the mean kinetic helicity and mean energy density of the turbulence. Below, we refer to the application of FOSA as the ‘standard prescription’.

An alternative treatment, suggested by Rogachevskii & Kleer (2000) and Blackman & Field (2002) was to replace the triple correlations which arise in the evolution equation for \mathcal{E} by a damping term proportional to \mathcal{E} itself (see BS05 for a review). Under this approximation, called the minimal- τ approximation (MTA) by BS05, one obtains, instead of (5), an evolution equation for \mathcal{E} , given by

$$\frac{\partial \mathcal{E}}{\partial t} = \frac{1}{\tau_c} (\alpha \overline{\mathbf{B}} - \eta_t \nabla \times \overline{\mathbf{B}}) - \frac{\mathcal{E}}{\tau}, \quad (7)$$

where again in the kinematic limit, α and η_t are given by Eq. (6) and τ is a relaxation time. For simplicity, this equation has been derived assuming that τ is scale-independent. When one takes into account the Lorentz force, the α -coefficient acquires an additional term proportional to the electric current helicity (Pouquet et al. 1976; Kleer & Ruzmaikin 1982; Gruzinov & Diamond 1994; Blackman & Field 2000; Rädler et al. 2003; BS05), and then

$$\alpha = \alpha_k + \alpha_m = -\frac{1}{3} \tau_c [\overline{\mathbf{u} \cdot \nabla \times \mathbf{u}} - \overline{\mathbf{b} \cdot \nabla \times \mathbf{b}}]. \quad (8)$$

The τ -approximation is motivated by the observation that if, hypothetically, the mean fields were suddenly switched off then one would expect the mean emf to decay gradually, over a finite damping time τ . This approximation has been tested in direct numerical simulations of forced turbulence (BS05; Brandenburg & Subramanian 2005b, 2007). These simulations of MTA find that τ is positive and the associated Strouhal number is of order unity, $\tau u_0 k_0 \simeq 1$, where k_0 is the wavenumber corresponding to the correlation scale of the random flow, and u_0 is its rms velocity. In principle, the damping or relaxation time τ can be different from the correlation time τ_c . For example, if τ_c is determined by the frequency with which expanding supernova shocks encounter a given point in space then it could be shorter than $\tau \simeq (u_0 k_0)^{-1}$ (Shukurov 2004). Thus, we keep the ratio $c_\tau = \tau/\tau_c$ as a dimensionless free parameter in the equations; for the numerical solutions we generally set it to unity. We then have

$$\left(\frac{\partial}{\partial t} + \frac{1}{\tau} \right) \mathcal{E} = \frac{c_\tau}{\tau} (\alpha \overline{\mathbf{B}} - \eta_t \nabla \times \overline{\mathbf{B}}). \quad (9)$$

If the explicit time derivative is neglected (valid if \mathcal{E} varies on timescales long compared to the relaxation time τ), and τ is approximated as τ_c , then (9) reduces to the expression (5) obtained from the standard prescription. An alternative way of arriving at Eq. (9) (with $c_\tau = 1$) is by keeping a time derivative of $\bar{\mathbf{B}}$ in the expression (5) for \mathcal{E} in order to introduce non-locality in time (Rheinhardt & Brandenburg 2012).

We now apply the mean-field approach to the induction equation with the MTA closure. Operating on Eq. (3) with $\partial/\partial t + 1/\tau$, using Eq. (9), assuming $\bar{\mathbf{U}}$ to be independent of time, and taking η and η_t to be spatially uniform, we arrive at

$$\left(\frac{\partial}{\partial t} + \frac{1}{\tau}\right) \frac{\partial \bar{\mathbf{B}}}{\partial t} = \nabla \times \left(\bar{\mathbf{U}} \times \frac{\partial \bar{\mathbf{B}}}{\partial t}\right) + \eta \nabla^2 \frac{\partial \bar{\mathbf{B}}}{\partial t} + \frac{1}{\tau} [\nabla \times (\bar{\mathbf{U}} \times \bar{\mathbf{B}} + c_\tau \alpha \bar{\mathbf{B}}) + (\eta + c_\tau \eta_t) \nabla^2 \bar{\mathbf{B}}].$$

After multiplying through by τ , this leaves us with an equation containing new terms proportional to τ (that do not emerge under the standard prescription),

$$\tau \frac{\partial^2 \bar{\mathbf{B}}}{\partial t^2} + \frac{\partial \bar{\mathbf{B}}}{\partial t} = \tau \nabla \times \left(\bar{\mathbf{U}} \times \frac{\partial \bar{\mathbf{B}}}{\partial t}\right) + \tau \eta \nabla^2 \frac{\partial \bar{\mathbf{B}}}{\partial t} + \nabla \times (\bar{\mathbf{U}} \times \bar{\mathbf{B}} + c_\tau \alpha \bar{\mathbf{B}}) + (\eta + c_\tau \eta_t) \nabla^2 \bar{\mathbf{B}}. \quad (10)$$

The same approach applied with the standard prescription gives the familiar result,

$$\frac{\partial \bar{\mathbf{B}}}{\partial t} = \nabla \times (\bar{\mathbf{U}} \times \bar{\mathbf{B}} + \alpha \bar{\mathbf{B}}) + (\eta + \eta_t) \nabla^2 \bar{\mathbf{B}}, \quad (11)$$

which is the $\tau \rightarrow 0$ limit of Eq. (10) with $c_\tau = 1$. Equation (10) contains a second-order, as well as first-order time derivatives, and belongs to the class of equations known as the telegraph equation (e.g., Courant & Hilbert 1989). The second time derivative can lead to wave-like properties, with $1/\tau$ as a damping coefficient. Unlike the mean induction equation (11), the telegraph equation (10) is not invariant under transformation to a rotating frame (see Paper II).

3 NUMERICAL SOLUTIONS

3.1 Method and approximations used

We now examine the evolution of the mean magnetic field numerically. We solve Eq. (10) when τ is finite, while Eq. (11) is solved for the case $\tau \rightarrow 0$. The components of Eq. (10) in cylindrical coordinates are given in Appendix A1. The saturation of the dynamo action is controlled by the helicity conservation, outlined in Appendix A2, together with the governing equations.

For convenience we define

$$\mathcal{F} \equiv \nabla \times \mathcal{E},$$

and assume that η , η_t , τ and c_τ are constants. The quantity \mathcal{F} has been introduced in addition to \mathcal{E} because this allows us to avoid having to impose boundary conditions on the components of \mathcal{E} and also to avoid applying the no- z approximation to the components of $\nabla \times \mathcal{E}$ (see below). Alternatively, we could have solved for the vector potential $\bar{\mathbf{A}}$ and \mathcal{E} , so the choice of using $\bar{\mathbf{B}}$ and \mathcal{F} is a matter of preference.

We make the thin-disc approximation, which implies $r^{-1} \partial/\partial \phi \ll \partial/\partial z$ and $\partial/\partial r \ll \partial/\partial z$. We also assume that the variation of the rotational and radial velocities along the z -axis is negligible. Then we can neglect $\bar{B}_z \partial \bar{U}_r / \partial z$ in the equation for \bar{B}_r and $\bar{B}_z \partial \bar{U}_\phi / \partial z$ in the equation for \bar{B}_ϕ . The thin-disc approximation and the condition $\nabla \cdot \bar{\mathbf{B}} = 0$ together imply that $|\bar{B}_z|/|\bar{\mathbf{B}}| \ll 1$. This approximation also allows us to ignore terms containing the ϕ - and r -derivatives of $\alpha \bar{B}_z$ in Eqs. (A4) and (A5), and of \bar{B}_z in Eqs. (A8) and (A9), as well as the term $\mathcal{E}_z \bar{B}_z$ in Eq. (A7) for α_m . Thus, the evolution equation for \mathcal{E}_z is no longer needed, and all terms containing \bar{B}_z are eliminated from all the relevant evolution equations. Once equations for \bar{B}_r and \bar{B}_ϕ are solved, we can obtain \bar{B}_z from $\nabla \cdot \bar{\mathbf{B}} = 0$ and \mathcal{F}_z from $\nabla \cdot \mathcal{F} = 0$. As a bonus, we do not have to worry about satisfying $\nabla \cdot \bar{\mathbf{B}} = 0$ and $\nabla \cdot \mathcal{F} = 0$ numerically.

Further, we write $\bar{U}_\phi = r\omega$, and take ω to be independent of ϕ . We also adopt $\bar{U}_r = 0$. However, a vertical velocity \bar{U}_z can be essential for the dynamo action, so it is retained. The vertical flow advects magnetic field as well as magnetic helicity (Shukurov et al. 2006). Crucially, a magnetic helicity flux away from the dynamo region is required to alleviate the catastrophic quenching of the α effect (BS05).

The no- z approximation (Subramanian & Mestel 1993; Moss 1995; Phillips 2001) is used as discussed in detail in Appendix B, to approximate the z -derivatives of the mean magnetic field. This reduces the three-dimensional problem to that in two dimensions (r and ϕ), thus greatly reducing the computational time required. The no- z approximation provides remarkably accurate solutions in one-dimensional dynamical quenching models (compare Shukurov et al. 2006 and Sur et al. 2007) and there are no reasons to doubt that it performs equally well in higher-dimensional problems. Under this approximation, \bar{U}_z represents a vertically averaged, mass-weighted vertical velocity.

3.2 Dimensionless governing equations

We adopt the length scale and rms velocity of the largest turbulent eddies to be $l = l_0 = 100$ pc and $u = u_0 = 10$ km s $^{-1}$, respectively. These parameters are taken to be constant in space and time. This leads to the following estimate for the turbulent diffusivity:

$$\eta_t = \eta_{t,0} \simeq \frac{1}{3} l_0 u_0 = 10^{26} \text{ cm}^2 \text{ s}^{-1}.$$

It is convenient to use dimensionless variables, with distance along the z -axis measured in the unit of the characteristic half-thickness of the disc h_0 , horizontal lengths measured in the radial disc scale length R , and time measured in typical vertical turbulent diffusion time $t_{d,0} = h_0^2/\eta_{t,0}$. We take as fiducial values $h_0 = 500$ pc and $R = 20$ kpc. For our purposes, it is not necessary to specify the magnetic field unit B_0 , so we leave it arbitrary. Thus, we have $l_0 = h_0/5$ and $u_0 = 15h_0 t_{d,0}^{-1}$ with $t_{d,0} \simeq 0.73$ Gyr.

Dimensionless variables, labelled with tilde, are thus introduced as $h = h_0 \tilde{h}$, $\eta_t = \eta_{t,0} \tilde{\eta}_t$, $r = R \tilde{r}$, $t = t_{d,0} \tilde{t}$, $\tau = t_{d,0} \tilde{\tau}$, $\omega = t_{d,0}^{-1} \tilde{\omega}$, $G = t_{d,0}^{-1} \tilde{G}$, $\alpha_k = h_0 t_{d,0}^{-1} \tilde{\alpha}_k$, $\alpha_m = h_0 t_{d,0}^{-1} \tilde{\alpha}_m$, $\bar{U}_z = h_0 t_{d,0}^{-1} \tilde{U}_z$, $B_{eq} = B_0 \tilde{B}_{eq}$, $\bar{\mathbf{B}} = B_0 \tilde{\mathbf{B}}$, $\mathcal{E} = B_0 h_0 t_{d,0}^{-1} \tilde{\mathcal{E}}$ and $\mathcal{F} = B_0 t_{d,0}^{-1} \tilde{\mathcal{F}}$. The quantities h_0 and R enter only in the ratios $\lambda = h_0/R$ and $K = 2(h_0/l_0)^2$. The rotational shear is denoted $G = rd\omega/dr$, and B_{eq} is a characteristic

field that may vary over space and time (normally associated with the equipartition field; see below). Then, dropping tildes, our set of equations can be written in dimensionless form as

$$\frac{\partial \overline{B}_r}{\partial t} = -\omega \frac{\partial \overline{B}_r}{\partial \phi} - \frac{\overline{U}_z \overline{B}_r}{h} + \mathcal{F}_r, \quad (12)$$

$$\frac{\partial \overline{B}_\phi}{\partial t} = G \overline{B}_r - \omega \frac{\partial \overline{B}_\phi}{\partial \phi} - \frac{\overline{U}_z \overline{B}_\phi}{h} + \mathcal{F}_\phi, \quad (13)$$

$$\begin{aligned} \frac{\partial \mathcal{F}_r}{\partial t} = & \tau^{-1} \left[-\frac{2c_\tau}{\pi h} \alpha \overline{B}_\phi - c_\tau \eta_t \frac{\pi^2}{4h^2} \overline{B}_r \right. \\ & \left. + c_\tau \eta_t \lambda^2 \left(\widehat{\mathcal{P}} \overline{B}_r - \frac{2}{r^2} \frac{\partial \overline{B}_\phi}{\partial \phi} \right) - \mathcal{F}_r \right], \end{aligned} \quad (14)$$

$$\begin{aligned} \frac{\partial \mathcal{F}_\phi}{\partial t} = & \tau^{-1} \left[-\frac{2c_\tau}{\pi h} \alpha \overline{B}_r - c_\tau \eta_t \frac{\pi^2}{4h^2} \overline{B}_\phi \right. \\ & \left. + c_\tau \eta_t \lambda^2 \left(\widehat{\mathcal{P}} \overline{B}_\phi + \frac{2}{r^2} \frac{\partial \overline{B}_r}{\partial \phi} \right) - \mathcal{F}_\phi \right], \end{aligned} \quad (15)$$

$$\frac{\partial \alpha_m}{\partial t} = -K \eta_t (\mathbf{E} \cdot \overline{\mathbf{B}} + \mathcal{R}_m^{-1} \alpha_m) - \frac{\alpha_m \overline{U}_z}{h} - \omega \frac{\partial \alpha_m}{\partial \phi}, \quad (16)$$

$$\frac{\partial \mathcal{E}_r}{\partial t} = \tau^{-1} \left(c_\tau \alpha \overline{B}_r - c_\tau \eta_t \frac{\pi}{2h} \overline{B}_\phi - \mathcal{E}_r \right), \quad (17)$$

$$\frac{\partial \mathcal{E}_\phi}{\partial t} = \tau^{-1} \left[c_\tau \alpha \overline{B}_\phi + c_\tau \eta_t \frac{\pi}{2h} \left(1 + \frac{3}{4\pi} \sqrt{\frac{-D}{\pi}} \right) \overline{B}_r - \mathcal{E}_\phi \right], \quad (18)$$

where

$$\widehat{\mathcal{P}} = -\frac{1}{r^2} + \frac{1}{r} \frac{\partial}{\partial r} + \frac{\partial^2}{\partial r^2} + \frac{1}{r^2} \frac{\partial^2}{\partial \phi^2},$$

$$\alpha = \alpha_k + \alpha_m, \quad K = 2 \left(\frac{h_0}{l_0} \right)^2,$$

$$\mathbf{E} \cdot \overline{\mathbf{B}} = \mathcal{E}_r \overline{B}_r + \mathcal{E}_\phi \overline{B}_\phi.$$

We have also neglected terms proportional to \mathcal{R}_m^{-1} in Eqs. (12) and (13), as $\mathcal{R}_m \gg 1$ in galaxies. We have retained such a term in Eq. (16); however, it can also be neglected if the flux is dominant, which is usually the case.

For $\tau \rightarrow 0$, these equations reduce to the three standard equations of the slab dynamo:

$$\begin{aligned} \frac{D \overline{B}_r}{Dt} = & -\frac{2c_\tau}{\pi h} \alpha \overline{B}_\phi - c_\tau \eta_t \frac{\pi^2}{4h^2} \overline{B}_r \\ & + c_\tau \eta_t \lambda^2 \left[\widehat{\mathcal{P}} \overline{B}_r - \frac{2}{r^2} \frac{\partial \overline{B}_\phi}{\partial \phi} \right], \end{aligned} \quad (19)$$

$$\begin{aligned} \frac{D \overline{B}_\phi}{Dt} = & G \overline{B}_r - \frac{2c_\tau}{\pi h} \alpha \overline{B}_r - c_\tau \eta_t \frac{\pi^2}{4h^2} \overline{B}_\phi \\ & + c_\tau \eta_t \lambda^2 \left[\widehat{\mathcal{P}} \overline{B}_\phi + \frac{2}{r^2} \frac{\partial \overline{B}_r}{\partial \phi} \right], \end{aligned} \quad (20)$$

$$\begin{aligned} \frac{D \alpha_m}{Dt} = & -K \eta_t \left[c_\tau \alpha (\overline{B}_r^2 + \overline{B}_\phi^2) + \mathcal{R}_m^{-1} \alpha_m \right. \\ & \left. + c_\tau \eta_t \frac{3\sqrt{-D}}{8\pi^{1/2} h} \overline{B}_r \overline{B}_\phi \right], \end{aligned} \quad (21)$$

where

$$\frac{D}{Dt} = \frac{\partial}{\partial t} + \omega \frac{\partial}{\partial \phi} + \frac{\overline{U}_z}{h}.$$

3.3 Initial and boundary conditions

The boundary conditions are $\overline{B}_r = \overline{B}_\phi = 0$ at $r = 0$ and $r = R$, where the former condition applies as long as we consider non-axisymmetric modes that are localized far away from the rotation axis. We need not impose boundary conditions on the other variables as their spatial derivatives are not present in the equations. This includes the components of \mathbf{E} , since they are only evaluated for the purpose of calculating $\mathbf{E} \cdot \overline{\mathbf{B}}$, but not for calculating the components of $\nabla \times \mathbf{E}$. In the azimuthal coordinate, \overline{B}_r and \overline{B}_ϕ , are subject to periodic boundary conditions, $\overline{B}_r|_{\phi=2\pi} = \overline{B}_r|_{\phi=0}$ and $\overline{B}_\phi|_{\phi=2\pi} = \overline{B}_\phi|_{\phi=0}$.

All variables vanish at $t = 0$ except for \overline{B}_r and \overline{B}_ϕ , whose seed values are chosen either to be Gaussian random fields for \overline{B}_r and zero for \overline{B}_ϕ , or to have the functional form

$$\overline{B}_\phi = \frac{r}{R} \left(1 - \frac{r}{R} \right)^2 e^{-r/R} (S_0 + S_1 \cos \phi), \quad (22)$$

$$\overline{B}_r = -\overline{B}_\phi, \quad (23)$$

where S_0 and S_1 are dimensionless constants that control the amplitudes (relative to B_0) of the $m = 0$ and $m = 1$ components of the seed field. The solenoidality condition $\nabla \cdot \overline{\mathbf{B}} = 0$ does not place any restriction on the form of the seed field, as \overline{B}_z can be obtained from $\nabla \cdot \overline{\mathbf{B}} = 0$. When we refer to the $m = 0$ seed, this means $S_0 = 1$ and $S_1 = 0$, while the $m = 1$ seed has $S_0 = 0$ and $S_1 = 1$.

The code uses sixth-order finite differences for the spatial derivatives and a third-order Runge–Kutta routine for the time derivatives, using the same algorithms as the publicly available PENCIL CODE¹.

3.4 The galaxy model

For the galactic rotation curve, we use the Brandt curve,

$$\omega(r) = \frac{\omega_0}{[1 + (r/r_\omega)^2]^{1/2}}, \quad (24)$$

where ω_0 and r_ω are parameters, so that with this profile, $\omega \rightarrow \text{const}$ as $r \rightarrow 0$ (solid body rotation) and $\omega \propto 1/r$ for $r \gg r_\omega$ (flat rotation curve). The rotational shear rate,

$$G(r) = r \frac{d\omega}{dr} = -\omega(r) \frac{(r/r_\omega)^2}{1 + (r/r_\omega)^2}, \quad (25)$$

tends to zero as $r \rightarrow 0$ and $G = -\omega$ for $r \gg r_\omega$, with the maximum magnitude of $2\omega_0/(3\sqrt{3})$ at $r = \sqrt{2}r_\omega$.

We model the disc half-thickness as a hyperboloid (RSS88),

$$h(r) = h_D [1 + (r/r_D)^2]^{1/2}, \quad (26)$$

where h_D is the scale height at $r = 0$ and r_D controls the disc flaring rate. With this form, $h \rightarrow h_D = \text{constant}$ as $r \rightarrow 0$ and $h \propto r$ for $r \gg r_D$.

We take the kinetic part of the α -coefficient to decrease with radius according to F. Krause's formula $\alpha_k \sim l^2 \omega/h$ (RSS88; BS05). For the models of non-axisymmetric disc, we also impose a spiral profile on α_k . For a rigidly rotating spiral, we use

$$\alpha_k(r, \phi) = \overline{\alpha}(r) \{1 + \epsilon_\alpha \cos[n(\phi - \Omega t) - \kappa r]\}, \quad (27)$$

¹ <http://pencil-code.googlecode.com> (Brandenburg 2003)

where the azimuthally averaged value of α_k , denoted with bar, is given by

$$\bar{\alpha}(r) = l^2 \omega(r)/h(r), \quad (28)$$

ϵ_α sets the degree of deviation from axial symmetry, n is the number of spiral arms, Ω is the angular velocity of the spiral pattern (i.e. the pattern speed), and κ , negative for a trailing spiral, determines how tightly the arms are wound. For a spiral winding up with the differential rotation of the gas, we take

$$\alpha_k(r, \phi) = \bar{\alpha}(r) [1 + \epsilon_\alpha \cos\{n[\phi + \phi_0 - \omega t']\}], \quad (29)$$

where we have included an arbitrary phase ϕ_0 and defined $t' = t - t_{\text{on}}$ where t_{on} is the time of onset of the α -spiral. We have also taken $\kappa = 0$, so that the α -spiral actually starts off as a ‘bar’ at $t' = 0$. Wherever necessary, we also require that $\alpha_k < u$.

The model also allows for a spiral modulation of the vertical advective velocity \bar{U}_z of a similar form:

$$\bar{U}_z = \bar{U}_{z,0} \{1 + \epsilon_U \cos[n(\phi - \Omega t) - \kappa r]\}, \quad (30)$$

where $\bar{U}_{z,0}$ is the azimuthally averaged value of \bar{U}_z .

Following other authors (e.g. RSS88) we define the turbulent magnetic Reynolds numbers to quantify the strengths of the differential rotation, α effect and vertical velocity:

$$R_\omega = Gh^2/\eta_t, \quad R_\alpha = \alpha_k h/\eta_t, \quad R_U = \bar{U}_z h/\eta_t.$$

The local dynamo number,

$$D = R_\alpha R_\omega = \alpha_k G h^3/\eta_t^2,$$

is a dimensionless measure of the intensity of the $(\alpha\omega)$ dynamo action at a given radius. For the mean field to grow due to the local $\alpha\omega$ -dynamo action alone, it is required that $D < D_{\text{cr}} \approx -10$ (RSS88, see also Paper II). In the limit $r \gg r_\omega$, an axisymmetric disc has $D \simeq -9(\omega h/u)^2$.

The functional form of the characteristic magnetic field is adopted as

$$B_{\text{eq}} = B_0 e^{-r/R}; \quad (31)$$

if appropriate, this can be identified with the magnetic field strength corresponding to the energy equipartition with the turbulence. Nonlinear dynamo effects are expected to become pronounced as soon as $|\bar{\mathbf{B}}| \simeq B_{\text{eq}}$.

3.5 Models explored and the representation of the results

The various numerical models considered here are summarized in Table 1. Many parameters are common to all models. For the disc scale length, we choose $r_D = R/2 = 10$ kpc and set its scale height to be $h = h_0 = 500$ pc at $r = R/2 = 10$ kpc, so that $h_D = h_0/\sqrt{2} = 354$ pc.

We adopt $r_\omega = 0.1R = 2$ kpc and set the circular speed to $\bar{U}_\phi = 375h_0 t_{\text{d},0}^{-1} = 250 \text{ km s}^{-1}$ at $r = R/2 = 10$ kpc, which gives $\omega_0 = 96t_{\text{d},0}^{-1} = 130 \text{ km s}^{-1} \text{ kpc}^{-1}$. This implies that $\omega = 18.75t_{\text{d},0}^{-1} = 25 \text{ km s}^{-1} \text{ kpc}^{-1}$, $G \simeq -18t_{\text{d},0}^{-1} = -24 \text{ km s}^{-1} \text{ kpc}^{-1}$, $\bar{\alpha} = 0.75h_0 t_{\text{d},0}^{-1} = 0.5 \text{ km s}^{-1}$ and the azimuthally averaged dynamo number $\bar{D} \simeq -13.5$ at $r = R/2 = 10$ kpc.

The resulting radial profiles of h , R_ω , R_α , and D are shown in Fig. 1.

Table 1. List of numerical models. Models A–D have an axisymmetric disc. The value of R_U given is its value at $r = R/2 = 10$ kpc, and, for Model F, its azimuthal average. ‘R’ in Column 2 indicates that the seed is Gaussian random noise in \bar{B}_r , whereas numbers 0 and 1 refer to the azimuthal symmetry of the seed field, $m = 0$ and $m = 1$, respectively. In Column 7, ‘T’ indicates that the imposed spiral is transient, while ‘W’ indicates that the α -spiral begins as a bar and winds up with the gas. In all models, runs were performed (i) without τ ($\tau \rightarrow 0$ limit), and (ii) with $\tau = l_0/u_0$. All models used $R = 40h_0 = 20$ kpc, as well as the profiles for the disc thickness and gas rotation velocity discussed in Section 3.4.

Model	Seed	l_0/h_0	R_U	ϵ_α	ϵ_U	$-\kappa R$	n
A	0	0.2	0	0	0	–	–
B	0	0.2	0.45	0	0	–	–
C	R	0.2	0.45	0	0	–	–
D	1	0.3	0.45	0	0	–	–
E	0	0.2	0.45	0.5	0	20	2
F	0	0.2	0.90	0	0.5	20	2
G	R	0.2	0.45	0.5	0	20	2
H	0	0.2	0	0.5	0	20	2
I	0	0.2	0.45	1	0	20	2
J	0	0.2	0.45	0.5	0	8	2
K	0	0.2	0.45	0.5	0	0	2
L	0	0.2	0.45	0.5	0	20	4
M	0	0.2	0.45	0.5	0	20,T	2
N	0	0.2	0.45	0.5	0	T,W	2

The corotation radius for models with steady spiral forcing is chosen as $r_{\text{cor}} = 8$ kpc, which is close to the observational estimates for the Milky Way (Gerhard 2011; Acharova et al. 2011). This leads to a pattern speed $\Omega = 23t_{\text{d},0}^{-1} = 31 \text{ km s}^{-1} \text{ kpc}^{-1}$. Moreover, a reasonable estimate for τ is given by $\tau = l_0/u_0 = (l_0^2/3h_0^2)t_{\text{d},0} = 0.013t_{\text{d},0}$. It is possible that τ is much smaller than our simple estimate for some galaxies and much larger for others. Therefore, we also consider the $\tau \rightarrow 0$ case, as well as $\tau = 2l_0/u_0$ and $\tau = 4l_0/u_0$ for some models.

We decompose each component of the mean magnetic field $\bar{\mathbf{B}}$ into a cosine Fourier series, with certain phases $\phi_{0,i}^{(m)}$ (see below),

$$\bar{B}_i(r, \phi, t) = \sum_{m=0}^{\infty} \tilde{B}_i^{(m)}(r, t) \cos\{m[(\phi - \phi_{0,i}^{(m)}(r, t))]\}, \quad (32)$$

where $i = r, \phi$, Thus,

$$\tilde{B}_i^{(0)} = \frac{1}{2\pi} \int_0^{2\pi} \bar{B}_i(r, \phi, t) d\phi, \quad (33)$$

and, for $m > 0$,

$$\tilde{B}_i^{(m)} = \frac{1}{\pi} \int_0^{2\pi} \bar{B}_i(r, \phi, t) \cos\{m[\phi - \phi_{0,i}^{(m)}(r, t)]\} d\phi. \quad (34)$$

The phase $\phi_{0,i}^{(m)}$ is obtained by trying all possible values and choosing the one which maximizes $\tilde{B}_i^{(m)}$. Using their phases, we also determine the rotation rates of the various Fourier modes by numerically differentiating the phase with respect to time.

The azimuthal average of the magnetic energy can be

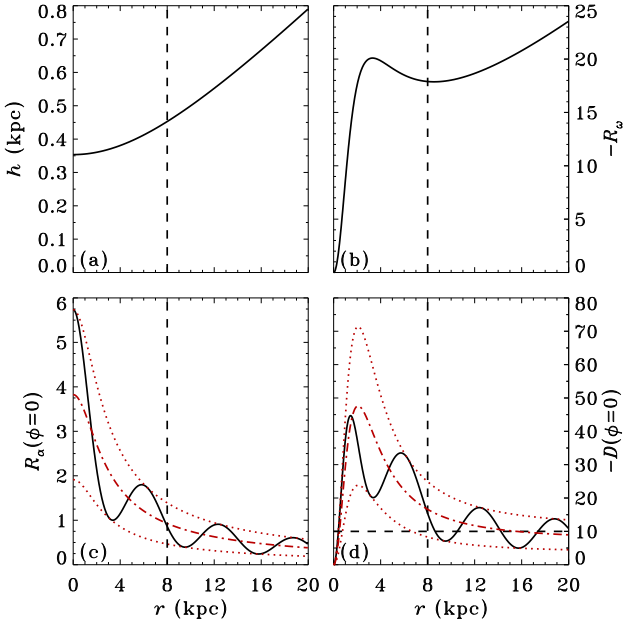


Figure 1. Inputs used for the basic non-axisymmetric Model E. (a) Disc scale height h , given by Eq. (26). (b) The dimensionless quantity $-R_\omega = Gh^2/\eta_t$ with G given by Eq. (25). (c) The dimensionless quantity $R_\alpha = \alpha_k h/\eta_t$, with α_k given by Eq. (27), at $\phi = 0$ (solid), azimuthal maximum/minimum (dotted), and azimuthal mean (dash-dotted). (d) Negative of the dynamo number $-D = -R_\alpha R_\omega$ at $\phi = 0$ (solid), along with its azimuthal extrema (dotted) and mean (dash-dotted). The azimuthal mean is used in axisymmetric models A-C. Negative of the approximate critical dynamo number $-D_{\text{cr}} \simeq 10$ is shown dashed for reference.

written as

$$\bar{E}(r, t) = \sum_{m=0}^{\infty} \tilde{E}^{(m)}(r, t), \quad (35)$$

where

$$\tilde{E}^{(0)}(r, t) = \frac{1}{8\pi} \left\{ \left[\tilde{B}_r^{(0)}(r, t) \right]^2 + \left[\tilde{B}_\phi^{(0)}(r, t) \right]^2 \right\}, \quad (36)$$

and, for $m > 0$,

$$\tilde{E}^{(m)}(r, t) = \frac{1}{16\pi} \left\{ \left[\tilde{B}_r^{(m)}(r, t) \right]^2 + \left[\tilde{B}_\phi^{(m)}(r, t) \right]^2 \right\}, \quad (37)$$

where the additional factor $1/2$ in the latter equation arises from averaging $\cos^2[m(\phi - \phi_{0,i}^{(m)})]$ over the interval $(0, 2\pi)$. Averaging over the area of the disc, we obtain the average magnetic energy in mode m ,

$$\langle \tilde{E}^{(m)} \rangle(t) = \frac{2}{R^2} \int_0^R \tilde{E}^{(m)}(r, t) r dr. \quad (38)$$

The numerical mesh used has $n_r = 200$ nodes in radius and $n_\phi = 120$ in azimuth for most runs, though for some runs we used $n_r = 100$ and $n_\phi = 60$.

4 DYNAMO IN AN AXISYMMETRIC DISC

A number of interesting questions can be addressed by considering dynamo action in an axisymmetric disc. One of them is how a whole young galaxy becomes magnetized with

a coherent field given that the radial diffusion time across a galaxy, $t_R \simeq R^2/\eta_t \simeq 3 \times 10^2$ Gyr, is typically larger than the age of the Universe. We examine this in the context of the dynamical quenching model of the galactic dynamo, using the no- z approximation.

4.1 Axisymmetric solutions

4.1.1 The role of the helicity flux

In local dynamo models (one-dimensional, retaining the z -dependence of the solution alone or zero-dimensional, using the no- z approximation) advection of magnetic helicity through the disc surface has been shown to alleviate the catastrophic nonlinear quenching of the dynamo (Shukurov et al. 2006; Sur et al. 2007). In the absence of any helicity flux, the mean magnetic field does grow to a fraction of the equipartition value, until α_m cancels α_k , after which magnetic field decays.

The result which obtains when the radial dimension is included is more interesting, even in the absence of a helicity flux. This case is studied using Model A (using the no- z approximation), with the evolution of the radial profile of the mean field strength shown in Fig. 2 for the case $\tau \rightarrow 0$. No notable differences exist between the $\tau \rightarrow 0$ and $\tau = l_0/u_0$ cases. For both cases, the kinematic global growth rate is virtually the same, $\Gamma = 5.7t_{d,0}^{-1} \simeq 7.8 \text{ Gyr}^{-1}$. Since the local growth rate of the field depends on the dynamo number, which in turn depends on r , the radius, the field maximum travels in radius. More specifically, the maximum is first localised where the dynamo number is the largest (r_M , say), but, at later time, at radii $r_M - \Delta r_1$ and $r_M + \Delta r_2$, etc. This leads to two rings of enhanced mean field, one moving inward and the other moving outward (the outer ring is more prominent in Model A). Because of the catastrophic α -quenching, the mean field eventually becomes negligible. (See Moss et al. (1998) for a discussion of propagating magnetic fronts in disc galaxies.)

On the other hand, if the vertical advection, and thus helicity flux, is above a certain threshold (but not too large), catastrophic quenching is averted. Then magnetic field can persist at about the same strength in a wide radial range, gradually spreading out until it occupies the entire region of the disc where the local dynamo number is supercritical. This is the situation illustrated with Model B, as shown in Fig. 3 ($\tau \rightarrow 0$ case), for $R_U = 0.45$ at $r = R/2 = 10 \text{ kpc}$ and $\bar{U}_z = 0.3 \text{ km s}^{-1}$ at all r . In this model, both $\tau \rightarrow 0$ and $\tau = l_0/u_0$ cases are again very similar, and the kinematic global growth rate for both cases is $\Gamma = 5.1t_{d,0}^{-1} \simeq 7.0 \text{ Gyr}^{-1}$. This is slightly smaller than for Model A, since the vertical flux removes large-scale magnetic field, rendering the dynamo less efficient in the kinematic stage. This model clarifies how the whole disc becomes magnetized. It does so by first reaching significant strengths in regions where the dynamo number is largest. Growth then saturates at each radius at a fraction of the local equipartition value, provided the vertical velocity (or helicity flux) is favourable for the dynamo action. The role of the radial diffusion is merely to couple the dynamo action at different radii as to lead to a magnetic structure growing at a single rate. Importantly, the entire disc becomes magnetized over a timescale much shorter than the radial diffusion time.

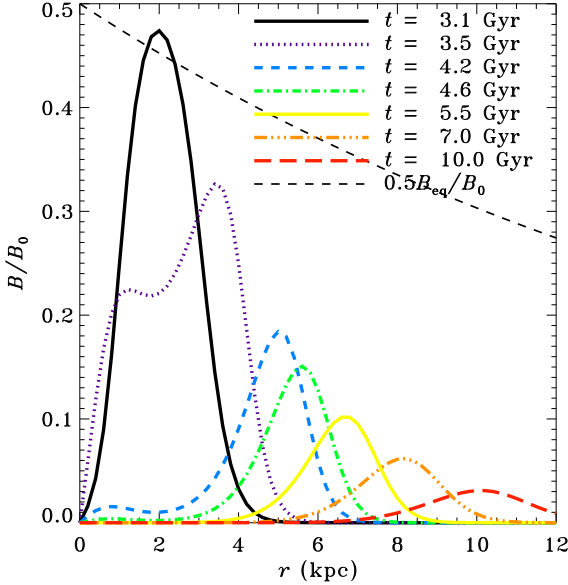


Figure 2. Evolution of the field strength $B = (B_r^2 + B_\phi^2)^{1/2}$ in Model A (axisymmetric disc, with $R_U = 0$). The mean field is confined to radially expanding and contracting rings.

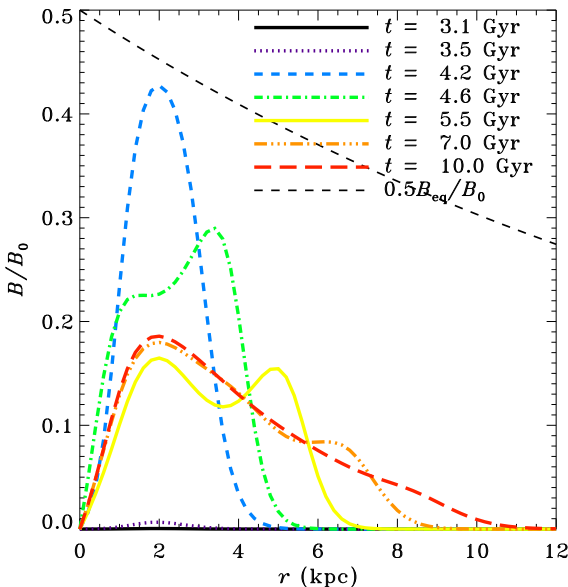


Figure 3. Evolution of the field strength in Model B (axisymmetric disc, with $R_U = 0.45 = 0.3 \text{ km s}^{-1}$). The mean field spreads radially to fill the disc.

4.2 Reversals of the magnetic field

If the seed magnetic field is weak enough, the steady-state magnetic configuration is independent of its form and strength. However, a relatively strong initial magnetic field can affect the steady-state magnetic configuration if nonlinear dynamo effects become important before the leading dynamo eigenfunction (normally represented by an axisymmetric magnetic field without any reversals along the radius)

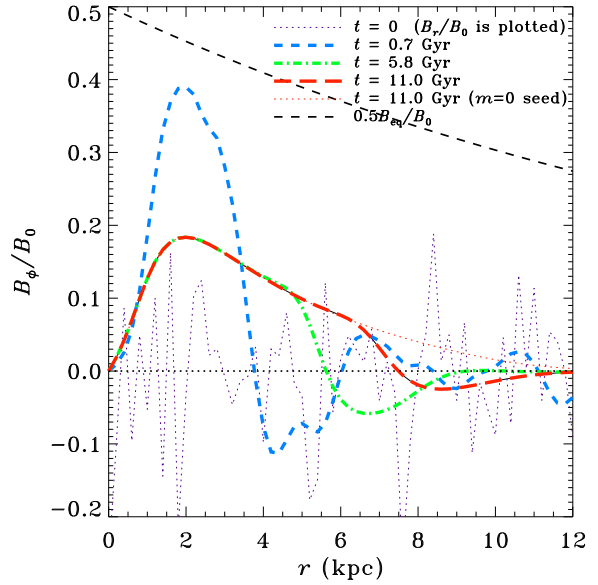


Figure 4. Evolution of the magnetic field that starts as a random seed magnetic field (Model C) in the $\tau \rightarrow 0$ case. Curves show \bar{B}_ϕ at the azimuth $\phi = 0$ at various times, with the exception of the field at $t = 0$, where \bar{B}_r is shown (since $\bar{B}_\phi = 0$). Otherwise, \bar{B}_r is omitted for the sake of clarity, but vanishes at the same set of radii as \bar{B}_ϕ , indicating reversals of the field at these locations. These reversals can survive for several Gyr, slowly moving outwards. For the final time, the solution obtained with an $m = 0$ seed is shown as a thin dotted line for reference.

can become dominant (Shukurov 2005; Moss et al. 2012). In particular, a random seed magnetic field can lead to long-lived reversals in the (quasi-)steady state magnetic configuration, either global (Poezd et al. 1993) or localised in both radius and azimuth (Bykov et al. 1997). A suitable random seed magnetic field can be readily provided by the fluctuation dynamo action (Poezd et al. 1993). Earlier results in this area have been obtained with a heuristic algebraic nonlinearity in the mean-field dynamo equation. Here we revisit this idea, but now with the physically motivated dynamic nonlinearity and finite τ .

In Model C, we have chosen a random seed specified as a two-dimensional Gaussian random field with the root-mean-square value of about one tenth the equipartition value (i.e., a fraction of μG in the Solar neighbourhood)² We also tried ten times larger seeds and found almost identical results. The number of radial grid points in this model is $n_r = 100$, corresponding to a resolution 0.2 kpc in radius, comparable to the correlation scale of the interstellar turbulence. The results are shown in Fig. 4. Firstly, large scale fields can develop over kpc scale regions, even in the outer disc, on Gyr timescales. More interestingly, it can be seen that reversals develop and persist for several Gyr in the nonlinear regime. (Because of the random nature of the problem, other random seeds of the same strength or different resolutions can result in field configurations without reversals.) The rever-

² The solenoidality of the seed field is ensured by an appropriate choice of \bar{B}_z .

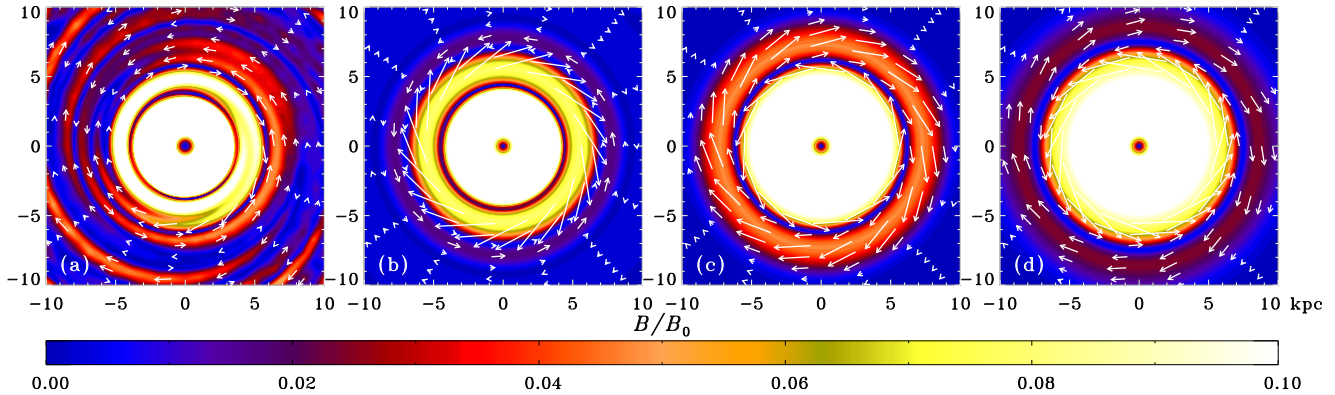


Figure 5. The strength of the mean magnetic field (colour coded) at (a) $t = 0.7$ Gyr, (b) 2.8 Gyr, (c) 7.3 Gyr, and (d) 11.0 Gyr in Model C (random seed field) for the case $\tau \rightarrow 0$. The colour of the central region has been saturated to enhance visibility of the magnetic structure in the outer disc. Field vectors are also shown, with tail length proportional to the magnitude of magnetic field, for $r > 5$ kpc only, to avoid clutter. Global reversals whose positions evolve with time are visible (for example, the central dark ring which moves out with time).

sals are also apparent in a time sequence of the magnetic field of Model C shown in Fig. 5. At least one reversal in the regular magnetic field has been observed in the Milky Way (Van Eck et al. 2011). It can be seen from both figures that as time goes on, the reversals become global in nature, propagate outward on a timescale of several Gyr, and in the process decrease in number. By $t = 6t_{d,0} = 4.4$ Gyr all reversals inside $r = 16$ kpc are global in nature (i.e. occur at all azimuth for a given radius). In the $\tau = l_0/u_0$ case, the noise from the random seed takes much longer to dissipate, and global reversals are only apparent much later on, at large radii where the field is very weak. The occurrence of the reversals and their sensitivity to model parameters need to be explored further. In particular, Poezd et al. (1993) found that the persistence of the reversals at the galactic lifetime scale strongly depends on the rotation curve. Our experiments reported here suggest that memory effects (finite τ) are also important.

4.3 Non-axisymmetric magnetic fields in an axisymmetric disc

To test the performance of our code with non-axisymmetric solutions, we have repeated several of the 2D kinematic-regime simulations of M96 with the same resolution (41 grid-points in r and 61 in ϕ), the same parameters, $R = 20h_0$, $\omega_0 t_d^{-1} = 10$, $r_\omega = 0.2R$, $R_\alpha = \text{const} = 1$, and without either disc flaring ($h = \text{const}$) or radial variation of the α effect, or the extra factors of $2/\pi$ and $\pi^2/4$ used to refine the no- z approximation elsewhere in this paper. M96 only considered axisymmetric and bisymmetric modes, $m = 0, 1$, to obtain their growth rates $\Gamma_0 = 0.80t_d^{-1}$ and $\Gamma_1 = 0.15t_d^{-1}$, respectively; the bisymmetric mode is localised near the edge of the disc and rotates at the rate $\Omega_1 = 2.46t_d^{-1}$. We confirm the existence of these modes and find good agreement with the results of M96. Our results are comfortably similar: $\Gamma_0 = 0.81t_d^{-1}$, $\Gamma_1 = 0.15t_d^{-1}$ and $\Omega_1 = 2.53t_d^{-1}$; the slight differences are likely due to the different algorithms used.

We note, however, that some conclusions of M96 may rely on the details of an oversimplified model that was used. In particular, the $m = 1$ mode grows because α_k is in-

dependent of r rather than being proportional to ω as in Krause's law. This allows the α effect to dominate over the rotational shear at large r , which favours the growth of non-axisymmetric modes as in α^2 versus $\alpha\omega$ dynamos (Raedler 1986). The factors $2/\pi$ and $\pi^2/4$ in the no- z approximation, absent in that model, reduce the α effect and enhance the importance of the turbulent diffusion, which also has an adverse effect on the growth of non-axisymmetric modes. We find that the non-axisymmetric modes decay in a more realistic model used here and for the parameters used in most of our numerical models (see Sect. 3.5). We also find, however, that the $m = 1$ mode can grow if we adopt somewhat modified parameters, e.g., a smaller rms turbulent velocity $u = 5 \text{ km s}^{-1}$ and a larger turbulent scale length $l = 150 \text{ pc}$. This makes sense because lowering u weakens the radial diffusion while increasing l enhances R_α , without affecting the shear. With this new set of parameters, α_k has to be truncated in the central region to ensure that $\alpha \leq \frac{1}{2}u$. The effect of the truncation is to shift the $m = 1$ mode to larger radius (near the peak of R_α) than it otherwise would be. It is worth noting that higher m modes are even more difficult to excite in an axisymmetric disc and would require the parameters to be more extreme still.

4.3.1 Nonlinear competition of non-axisymmetric modes

In Model D, we focus on the case $\tau \rightarrow 0$. The $m = 1$ mode is readily excited with the kinematic growth rate $\Gamma_1 = 1.7t_{d,0}^{-1}$. The growth rate for the axisymmetric mode for these parameters is $\Gamma_0 = 4.7t_{d,0}^{-1}$. Since $\Gamma_0 > \Gamma_1$ with a significant margin, magnetic field in a mature dynamo hosted by an axisymmetric disc will be axisymmetric unless the seed magnetic field is strongly non-axisymmetric. The latter is, in fact, quite plausible if the seed field arises, for example, from a putative intergalactic field captured as the disc galaxy forms. In order to address this point, we have run Model D, starting from a purely $m = 1$ seed, with the $m = 0$ mode being seeded only by the numerical noise, as in M96. We adjust the strength of the seed such that nonlinear dynamo effects become significant at various important stages: (i) when the

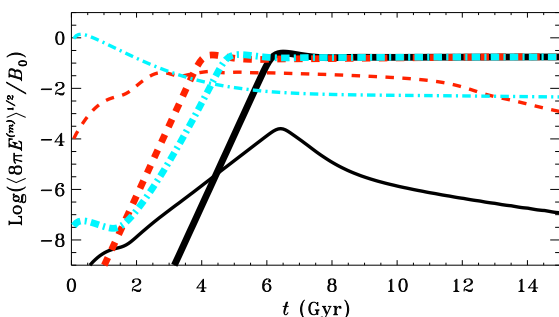


Figure 6. Evolution of the normalised magnetic field strength averaged over the disc, in the $m = 0$ (thick) and $m = 1$ (thin) modes, for a purely bisymmetric ($m = 1$) seed magnetic field (Model D). Different line styles show three cases with identical parameters, except for the magnitude of the seed field, so that the dynamo action saturates (i) when the $m = 0$ mode dominates (solid), (ii) when $m = 1$ dominates (dashed), and (iii) right from $t = 0$ (dash-dotted). Only in case (ii) does a significant $m = 1$ component survive for several Gyr.

$m = 0$ mode has already come to dominate, (ii) when it is still weaker than the $m = 1$ mode, and (iii) right from $t = 0$.

The results are shown in Fig. 6. Thick lines correspond to the normalised magnetic field strength (averaged over the area of the disc) in the $m = 0$ mode while thin lines correspond to that in the $m = 1$ mode. In Case (i), shown by the solid lines, the saturation of the (essentially axisymmetric) field clearly causes the $m = 1$ mode to decay since its growth requires a stronger (unquenched) dynamo action.

In Case (ii) (dashed lines), the early saturation of the (stronger) $m = 1$ mode still does not prevent the $m = 0$ mode from growing and evolving as in Case (i). This happens because the magnetic field in between the extrema of the non-axisymmetric magnetic field remains relatively weak when the $m = 1$ mode ceases to grow. Therefore, the growing $m = 0$ mode is supported by the local dynamo action in those regions, to fill the gaps until the field is saturated everywhere to become nearly axisymmetric. However, the $m = 1$ mode, though subdominant, does not immediately decay but remains strong for several Gyr. This feature can be understood from Fig. 7, which shows snapshots of \bar{B}_ϕ/B_0 at various times. Initially, the $m = 1$ mode is growing exponentially. Like the axisymmetric mode in Case (i), the $m = 1$ mode begins to spread radially as soon as nonlinear effects become important. At any given radius, the $m = 0$ mode eventually catches up and begins to dominate there. Thus, the outward spreading of the dominant $m = 0$ mode is preceded by the outward spreading of the $m = 1$ mode. As a result, a ring of $m = 1$ is formed (blue and red spirals in Fig. 7), surrounding a central disc of $m = 0$, both expanding outward with time. Eventually, the axisymmetric mode comes to dominate everywhere and the $m = 1$ decays more quickly (for $t \gtrsim 12$ Gyr).

In Case (iii) (dash-dotted lines), we find that the $m = 1$ mode first decays and then remains much weaker than the $m = 0$ mode.

As far as the overall survival of non-axisymmetric modes in an *axisymmetric* disc is concerned, we can conclude that:

(i) a rather special parameter combination is needed for a non-axisymmetric mode to grow;

(ii) for a non-axisymmetric mode to persist for several Gyr in the nonlinear stage, it must reach the saturation strength before the $m = 0$ can do so; given that non-axisymmetric modes have smaller growth rates, this implies that they must be much stronger initially;

(iii) in any case, all non-axisymmetric modes eventually decay in an axisymmetric disc.

These conclusions make it all the more reasonable to suggest that deviations from perfect axial symmetry of the underlying disc are required to explain the prevalence of non-axisymmetric regular fields in many galaxies. It is the mechanism of ‘spiral forcing’ of the dynamo to which we now turn.

5 MAGNETIC ARMS ENSLAVED TO A STATIONARY SPIRAL PATTERN

In this section, we consider the evolution of the mean magnetic field in a non-axisymmetric disc where the α effect is modulated by a stationary spiral pattern. As above, our analysis includes the dynamic nonlinearity, thus extending fully into the saturated states of the dynamo action, and allows for a finite dynamo relaxation time τ . The results at the kinematic stage can be compared with the semi-analytical solutions of Paper II.

As a consistency check, we have first made sure that the standard dynamo solutions, obtained by solving Eq. (11) are obtained when solving Eq. (10) with τ approaching zero. Indeed, we found good agreement with them for $\tau = 10^{-3}$. To ensure that the results are not sensitive to the location of the outer boundary, we compared solutions with outer radius of $R = 15$ kpc and 30 kpc, with the standard value $R = 20$ kpc (with the radial resolution modified proportionately). The results are not sensitive to this adjustment.

Our standard model is labelled F, with parameters given in Table 1. To explore the parameter space, we have also considered Models F–L.

5.1 Kinematic solutions

The evolution of the normalized magnetic field strength in various even- m modes, averaged over the area of the disc, is shown, for Model E, in Fig. 8. In the kinematic regime, all modes have about the same growth rate $\Gamma \simeq 5.1t_{d,0}^{-1} \simeq 7.0 \text{ Gyr}^{-1}$ for both $\tau \rightarrow 0$ and $\tau = l_0/u_0$ cases. This growth rate is also in close agreement with the growth rate for the axisymmetric case (Model B). This is not surprising because the average field in the disc is used to calculate the growth rate, and the field is dominated by the contribution at $r \ll r_{\text{cor}}$, where non-axisymmetric modes are negligible. The even- m modes grow together with the $m = 0$ mode because they are driven by (enslaved to) it. The $m = 2$ and $m = 4$ modes corotate with the spiral pattern. The odd modes are so weak that they are dominated by numerical noise, and thus also grow with the $m = 0$ mode.

We illustrate in Fig. 9 various aspects of the solution at $3t_{d,0}$ after the simulation has begun (or $t = -5.8$ Gyr in the plots), when the dynamo is still in the kinematic regime, and

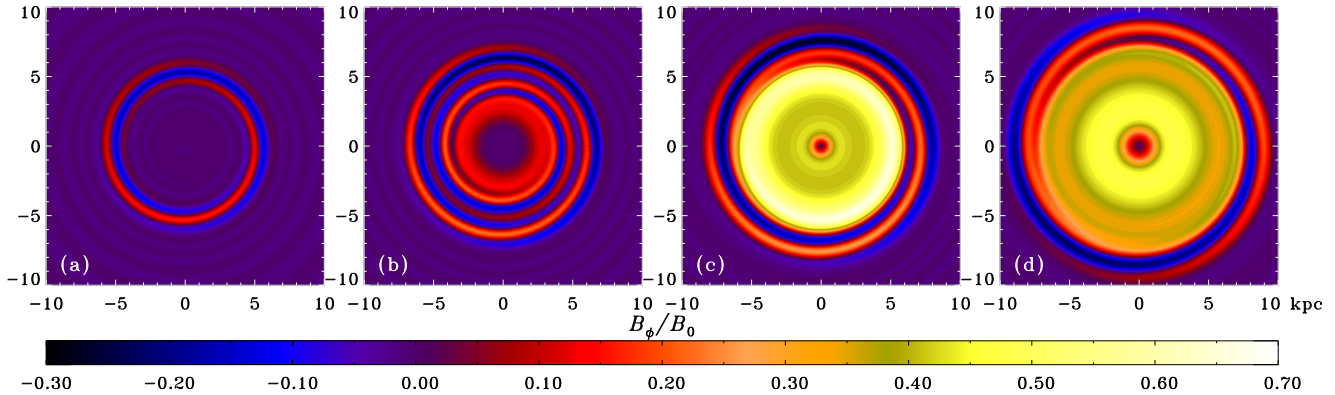


Figure 7. The ϕ -component of the magnetic field in Model D, i.e. an $m = 1$ seed field in an axisymmetric disc, at (a) $t = 2.2$ Gyr, (b) 3.7 Gyr, (c) 5.1 Gyr, and (d) 6.6 Gyr. The results shown are for Case (ii), as described in the text, with the initial average strength of the $m = 1$ mode of about $10^{-4}B_0$ (dashed curves in Fig. 6). The bisymmetric ($m = 1$) mode survives for several Gyr in the nonlinear regime in the form of an expanding annulus surrounding an expanding $m = 0$ disc.

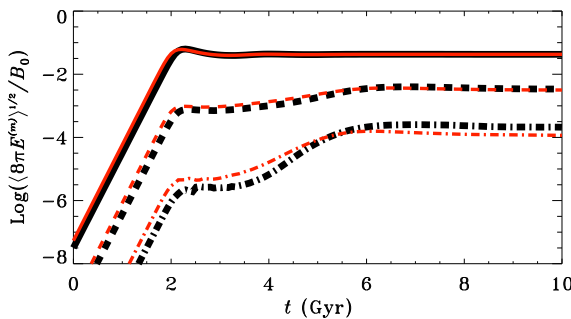


Figure 8. Magnetic field strength in the $m = 0$ (solid), $m = 2$ (dashed) and $m = 4$ (dash-dotted) modes of the mean magnetic field, averaged over the entire disc and normalized to B_0 , the equipartition field strength at $r = 0$, for Model E. Results obtained for $\tau = l_0/u_0$ are shown in thick black, while those for $\tau \rightarrow 0$ are in thin red. All modes have exponential kinematic growth rate $\Gamma^{(m)} = 7.0$ Gyr $^{-1}$. For the convenience of presentation, time has been rescaled so that the simulation in fact starts from $t = -8$ Gyr (not shown).

one can compare these results with the semi-analytical solutions of Paper II. In Fig. 9a, \overline{B}_ϕ (solid) and \overline{B}_r (dashed) have been plotted for both $\tau \rightarrow 0$ (red) and $\tau = l_0/u_0$ (black) cases, at $\phi = \phi_{\text{cor}}$, one of the two azimuthal angles where the α -spiral crosses the corotation circle. As expected, the field is strongest inside the corotation radius, where the magnitude of the dynamo number is largest – this is clear from Fig. 9a. Importantly, however, there is an excess of magnetic energy near the corotation radius, as compared to what is obtained in an axisymmetric disc, mainly due to the presence of strong additional $m = 0$ and $m = 2$ components near $r = r_{\text{cor}}$. The $m = 4$ component of the field is found to always be much weaker than $m = 2$.

The presence of the non-axisymmetric component near corotation can be more clearly seen in Fig. 9b. There we plot the ratio of the non-axisymmetric part of B_ϕ to the

axisymmetric part,

$$\delta = \frac{B_\phi - B_\phi^{(0)}}{B_\phi^{(0)}}.$$

at the azimuth $\phi = \phi_{\text{cor}}$. For both vanishing and finite τ , the eigenfunction is important within an annulus of width ≈ 4 kpc, centred near the corotation circle. Note that in both cases, the radial phase varies much more rapidly than that of α (plotted as a thin dash-dotted line in the figure). This indicates that the magnetic arms are much more tightly wound than the material arms. The effect of a finite τ is to strengthen the non-axisymmetry, and also to slightly increase the variation of the radial phase. In addition, the eigenfunction extends out to somewhat larger radius in the $\tau = l_0/u_0$ case than it does for $\tau \rightarrow 0$. This is illustrated by the second maximum with $\delta > 0$ at $r \simeq 10$ kpc that occurs when $\tau = l_0/u_0$, and is caused by the tail of the spiral magnetic field wrapping around an extra half-circle from where it crosses the corotation circle. Also shown in Fig. 9b as dashed lines is the envelope of the solid lines as ϕ changes.³

The difference between the azimuthal positions where \overline{B}_ϕ (or \overline{B}_r) and α are maximum, denoted Δ_ϕ (or Δ_r), are shown in Fig. 9c. Positive values of these quantities imply that the magnetic arms lead the material arms, while negative values imply that they trail them. The position r_{max} of the global maximum of δ (maximum of the dashed envelope in Fig. 9b), which is the radius at which the non-axisymmetric component of the field is most important relative to the axisymmetric component, is indicated with a vertical dotted line (red for $\tau \rightarrow 0$ and black for $\tau = l_0/u_0$): $r_{\text{max}} \simeq 8.3$ kpc for $\tau \rightarrow 0$ and 8.7 kpc for $\tau = l_0/u_0$. One can see that r_{max} is nearer r_{cor} for $\tau \rightarrow 0$ than for $\tau = l_0/u_0$.

In the $\tau \rightarrow 0$ case, studied by MS91 and SM93, it was found that $\Delta_\phi = \Delta_r = 0$ at $r = r_{\text{cor}}$ and $r_{\text{max}} = r_{\text{cor}}$, i.e. magnetic and material arms intersect at the corotation radius, and magnetic arms are strongest there. Therefore, magnetic arms go from leading the α -spiral in the sense of

³ The envelope is not perfectly symmetrical about $\delta = 0$ because of interference between the $m = 2$ mode and the much smaller $m = 4$ mode.

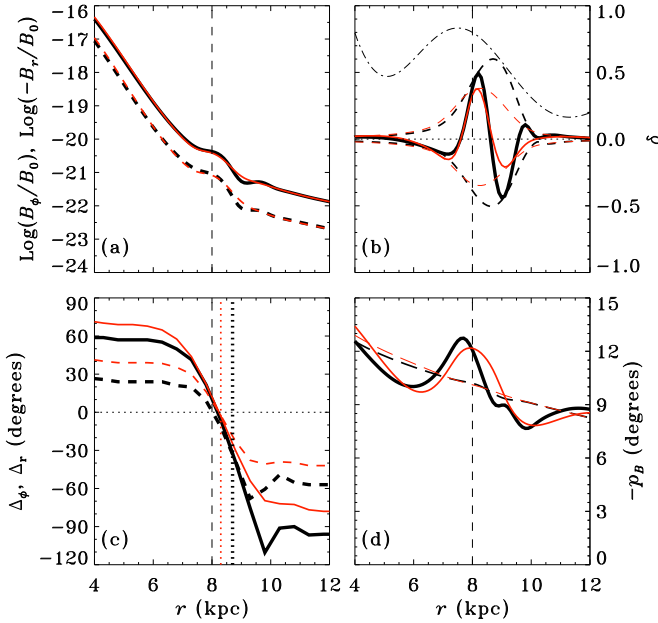


Figure 9. Properties of the field in the kinematic regime for Model E at a time $3t_{d,0}$ after the simulation is begun. Thick black illustrates the $\tau = l_0/u_0$ case while thin red illustrates $\tau \rightarrow 0$. In all plots, the corotation radius is shown as a dashed vertical line. **a)** The normalized azimuthal (solid) and radial (short dashed) components of the field at the azimuth $\phi = \phi_{\text{cor}}$ for which the α -spiral crosses corotation. **b)** The ratio δ of the non-axisymmetric to axisymmetric ϕ -component of the field at ϕ_{cor} (solid), and at azimuthal extrema (dashed). The quantity $\alpha_k(r, \phi_{\text{cor}})$ is shown as a thin dash-dotted line for reference. **c)** The phase of the ϕ -component (solid) or r -component (dashed) of the magnetic spiral minus the phase of the α -spiral (smoothed over 5 radial grid points, or 100 pc). The radius r_{max} at which the global maximum of δ occurs is plotted as a vertical dotted line for each τ case. **d)** Negative of the pitch angle at $\phi = \phi_{\text{cor}}$ (solid), with azimuthal mean (dashed).

the rotation for $r < r_{\text{cor}}$, to trailing it for $r > r_{\text{cor}}$. In the vanishing τ case in our model, r_{max} is slightly larger than r_{cor} , and Δ_ϕ and Δ_r are not precisely zero at r_{max} nor at r_{cor} . These differences between the results of our initial value treatment and those of the eigenvalue treatment of those authors can be attributed to interference from the dominant axisymmetric eigenmode, which is concentrated at smaller radius near where the dynamo number peaks, in our model. In any case, for both $\tau \rightarrow 0$ and $\tau = l_0/u_0$, the magnetic and α -spiral arms intersect in the vicinity of corotation, and the magnetic arms are also strongest in the vicinity of corotation, as in the earlier models.

What is more noteworthy, however, is the phase shift in the magnetic arms produced by a finite dynamo relaxation time. This is best evaluated by comparing the values of Δ_ϕ and Δ_r at the radius r_{max} (which itself depends on τ), where the magnetic arms are strongest. (Since \overline{B}_ϕ dominates over \overline{B}_r , Δ_ϕ is more important than Δ_r , but in the vicinity of the corotation radius, where non-axisymmetry is important, $\Delta_\phi \simeq \Delta_r$.) We find $\Delta_\phi(r_{\text{max}}) \simeq \Delta_r(r_{\text{max}}) = -3^\circ$ for $\tau \rightarrow 0$ and -30° for $\tau = l_0/u_0$, for an overall phase shift of -27° . This is comparable in magnitude to the value $\Omega\tau = 18^\circ$ that results from an order of magnitude estimate of the phase

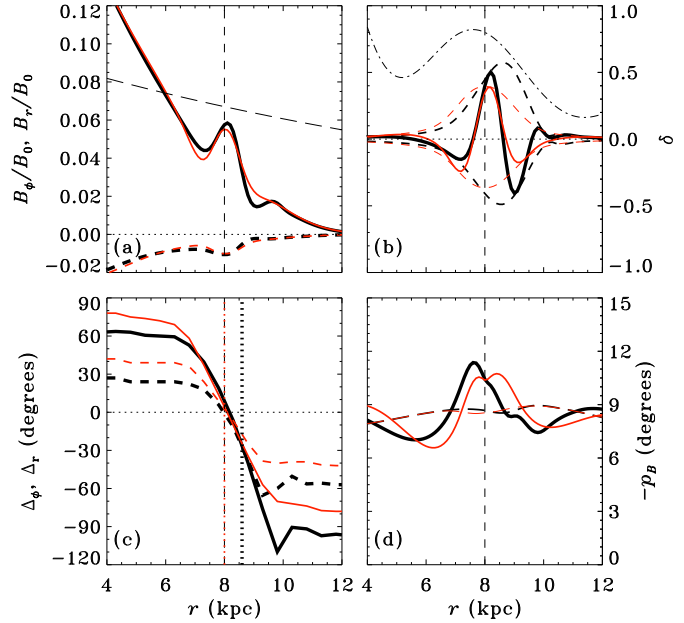


Figure 10. As Fig. 9 (Model E), but now for $t = 10$ Gyr (see Fig. 8), when the field has reached equilibrium as a result of dynamical quenching. Note that in (a) The scale is now linear instead of logarithmic. The long dashed curve is equal to $0.1B_{\text{eq}}/B_0$, shown for reference. An enhancement is evident near corotation in the saturated state.

shift. As mentioned earlier, non-locality in time produces a delay in the α effect of order τ , so that the α -spiral has rotated through an angle $\approx \Omega\tau$ before the dynamo has had the chance to respond to it. We recall that a phase shift of $\pm 90^\circ$ would correspond to peaks of the magnetic arms located mid-way between the spiral arms of α .

The magnetic pitch angle

$$p_B = \arctan \frac{\overline{B}_r}{\overline{B}_\phi}$$

is plotted (by magnitude) in Fig. 9d, with its azimuthal mean shown as a dashed line. The negative value of p_B indicates that magnetic lines have the form of a trailing spiral. The magnitude of p_B is larger along the α -spiral, which is expected since \overline{B}_r is produced more efficiently where α is larger. The azimuthally averaged value of $|p_B|$ decreases with radius such that $\tan p_B \propto 1/h$, as expected (Ruzmaikin et al. 1988; Shukurov 2005).

In the kinematic stage, various eigenmodes are competing until the eigenfunction eventually gets smoothed out by the radial diffusion and grows uniformly with the global growth rate Γ . As a consequence, the excess seen near the corotation radius in Fig. 9a becomes less and less apparent with time (but returns in the saturated state, see below). Furthermore, the values of r_{max} gradually increase before settling down (by $\simeq 7t_{d,0}$ after the simulation has begun) at $r_{\text{max}} = 9.3$ kpc for $\tau \rightarrow 0$ and $r_{\text{max}} = 9.5$ kpc for $\tau = l_0/u_0$. The key results mentioned, in particular the large phase shift caused by a finite dynamo relaxation time, are valid for any time during the kinematic regime.

5.2 Magnetic arms in the nonlinear dynamo

Many of the features of the kinematic solution are also apparent in the nonlinear regime. Figure 10 is similar to Fig. 9, but now for the saturated dynamo. In Fig. 10a, it can be seen that nonlinear effects significantly enhance the $m = 2$ part of the mean magnetic field near the corotation radius. In Fig. 10b, it is clear that deviations from axisymmetry are only important within $\approx \pm 2$ kpc of the corotation radius, and that the corresponding eigenfunction is strongly peaked about the corotation circle. Fig. 10c shows the phase shifts Δ_ϕ and Δ_r , with the location of the global maximum r_{\max} of δ shown as a dashed vertical line (red for $\tau \rightarrow 0$ and black for finite τ). In this case, $r_{\max} \simeq 8.0$ kpc for $\tau \rightarrow 0$ (consistent with the corotation radius) and $r_{\max} \simeq 8.6$ kpc for $\tau = l_0/u_0$. Because the eigenfunction is sharply peaked, it is more useful to consider the values of Δ_ϕ and Δ_r at r_{\max} rather than their asymptotic values far from corotation. The phase differences $\Delta_r(r_{\max})$ and $\Delta_\phi(r_{\max})$ are $+3^\circ$ when $\tau \rightarrow 0$ and -27° for $\tau = l_0/u_0$. Thus, the non-axisymmetric parts of the magnetic field are substantially displaced from the α -spiral arms by an overall phase shift of -30° due to the finite value of τ . The magnitude of the displacement is again comparable to $\Omega\tau = 18^\circ$, as expected. Fig. 10d shows the magnitude of the pitch angle at $\phi = \phi_{\text{cor}}$ as well as the azimuthal mean of this quantity for both τ cases. When comparing to the dash-dotted curve illustrating α_k at $\phi = \phi_{\text{cor}}$ in panel (b), it is clear that, like in the kinematic regime, the magnitude of the pitch angle is generally larger along the α -spiral. However, the decreasing trend $p_B \propto 1/h$ is no longer present in the nonlinear regime, and the azimuthal average of p_B (dashed curve) is almost constant over a large range of radius for both τ cases.

Figure 11 shows the magnetic field strength (upper panels), the quantity δ (middle panels), and pitch angle (lower panels) obtained in Model E, with the case of $\tau \rightarrow 0$ on the left, $\tau = l_0/u_0$ in the middle column, and $\tau = 2l_0/u_0$ on the right. The upper panels contain information similar to that of Fig. 10a, the middle row of panels are similar to Fig. 10b, while the lower panels are similar to Fig. 10d. In the upper panels, which show the field magnitude, magnetic arms are clearly visible near the corotation circle. As they are more tightly wound than the α -arms, they cut across them, as noted above. Comparing panels (a)–(c) or (d)–(f) of Fig. 11, and also the black and red curves of Fig. 10b, we may note the changes to the magnetic field caused by a finite τ , particularly outside of the corotation circle. The magnetic arms are more pronounced (larger \bar{B} at their centres), are more sharply defined (faster variation of the radial phase), and can be seen to extend for a longer azimuthal angle outside of the corotation circle for the finite τ case compared to the $\tau \rightarrow 0$ case. Since the mean electromotive force responds to an enhancement in α with a time delay τ , the maxima in magnetic field strength are displaced downstream from those of α by an angle of order $\Omega\tau$. Moreover, in the $\tau = l_0/u_0$ case, a more significant part of the magnetic arm clearly lies in between the α -spiral arms. These features can be seen more clearly for $\tau = 2l_0/u_0$ in the right hand panels of Fig. 11. As τ is increased, the downstream (trailing the α -spiral) part of the magnetic arms becomes more and more extended, whereas the upstream part is suppressed.

The magnitude of the pitch angle is displayed in the

lower panels of the figures, and clearly also has a spiral pattern. The pitch angle, as opposed to the field magnitude, does not vary strongly with radius. Because of this, the spiral morphology of the field is more clearly visible in the pitch angle. However, an accuracy of a few degrees would be required to measure the differences.

Another quantity that can be obtained is the pitch angle of the magnetic ridges, i.e. of the magnetic arms themselves as opposed to the magnetic field that constitutes them. This can then be compared with the pitch angle of the α -spiral arms. To estimate the pitch angle of the α -spiral, from Eq. (27), we may write down an expression for the values of azimuth (along one of the n arms) ϕ_{\max} which maximize α_k ,

$$\phi_{\max} = \frac{\kappa r}{n} + \Omega t. \quad (39)$$

The pitch angle p_α of the alpha spiral can then be obtained using the expression

$$\cot p_\alpha = r \frac{\partial \phi_{\max}}{\partial r} = \frac{\kappa r}{n}. \quad (40)$$

Substituting the values from Model E, $\kappa = -20R^{-1}$, $n = 2$, as well as $r = r_{\text{cor}} = 0.4R$, we obtain $p_\alpha(r_{\text{cor}}) = -14^\circ$.

Now we obtain the pitch angle of the magnetic ridges. We define a ridge as the spiral connecting the maxima of the magnetic energy E , or, equivalently, the field magnitude. Using the same approach as in Eq. (40) above, the pitch angle p_E of one such ridge can be written as

$$\cot p_E = \frac{\kappa r}{n} + r \frac{\partial \Delta_E}{\partial r}, \quad (41)$$

where the phase shift Δ_E of the ridge with respect to the α -spiral is analogous to the quantities Δ_r and Δ_ϕ discussed above. We evaluate the pitch angles at $r = r_{\max}$, where the global maximum of the quantity δ is located, recalling that $r_{\max} = 8.0$ kpc for $\tau \rightarrow 0$, while $r_{\max} = 8.6$ kpc for $\tau = l_0/u_0$. We then find $p_E(r_{\max}) \simeq -5^\circ$ for $\tau \rightarrow 0$, and $p_E(r_{\max}) \simeq -4^\circ$ for $\tau = l_0/u_0$. The pitch angles of the magnetic ridges are quite small, even as compared to the rather tightly wound α -spiral. One must keep in mind, however, that the values obtained for p_E are sensitive to the shear near corotation.

5.3 Coupling of the spiral pattern to galactic dynamos: multitude of mechanisms

Modulation of the α effect is just one of the mechanisms through which the spiral pattern can affect the dynamo action. In this section we consider two other plausible mechanisms in more detail, which eventually have to be combined into a conclusive picture.

5.3.1 Outflow speed modulated by the spiral pattern

Model F has the vertical advection velocity enhanced along a spiral (with the α -spiral turned off), to model stronger galactic outflows from the spiral arm regions, where star formation is enhanced. We use $R_U = 0.90$ at $r = R/2 = 10$ kpc and $\epsilon_U = 0.5$ so that the outflow speed within the arms, corresponding to $R_U = 1.35$, is too large for the optimal field growth near corotation, while the inter-arm value of

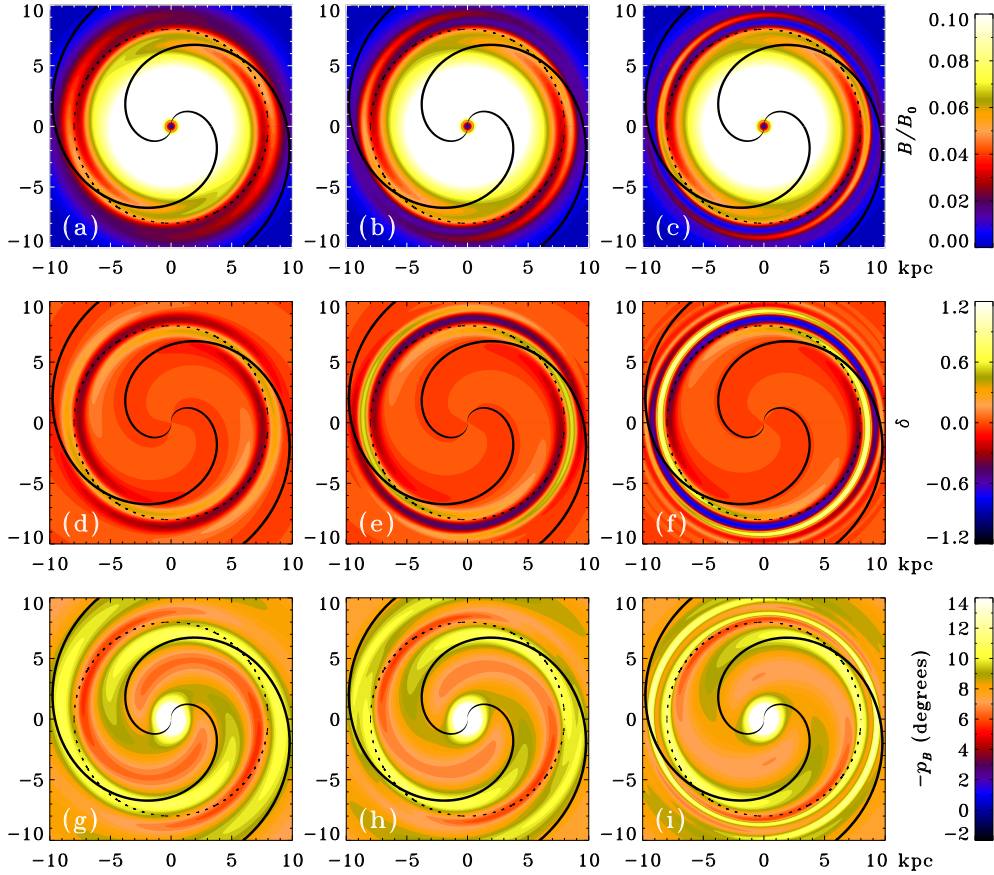


Figure 11. The top panels (a)–(c) show the magnitude of the magnetic field in the saturated state ($t = 10$ Gyr) in the $\tau \rightarrow 0$ (left), $\tau = l_0/u_0$ (middle) and $\tau = 2l_0/u_0$ (right) cases. In all panels, the peak of α_k is shown as a thick black line, while the corotation radius is illustrated as a black dotted circle. The colour of the central regions in (a)–(c) has been saturated in order to visually bring out the behaviour near corotation, where the non-axisymmetric modes are important. Panels (d)–(f) show the ratio δ of the non-axisymmetric to axisymmetric components of \bar{B}_ϕ . It can be seen that the τ effect acts to enhance the non-axisymmetry in the field. It also causes a phase shift of the magnetic arms toward the trailing side of the material arms, leading to magnetic arms that are more pronounced in the region between the material arms than for the $\tau \rightarrow 0$ case. The bottom panels show the magnetic pitch angle. Again, the colour within a region around the center has been saturated to render the non-axisymmetry of the pitch angle more apparent.

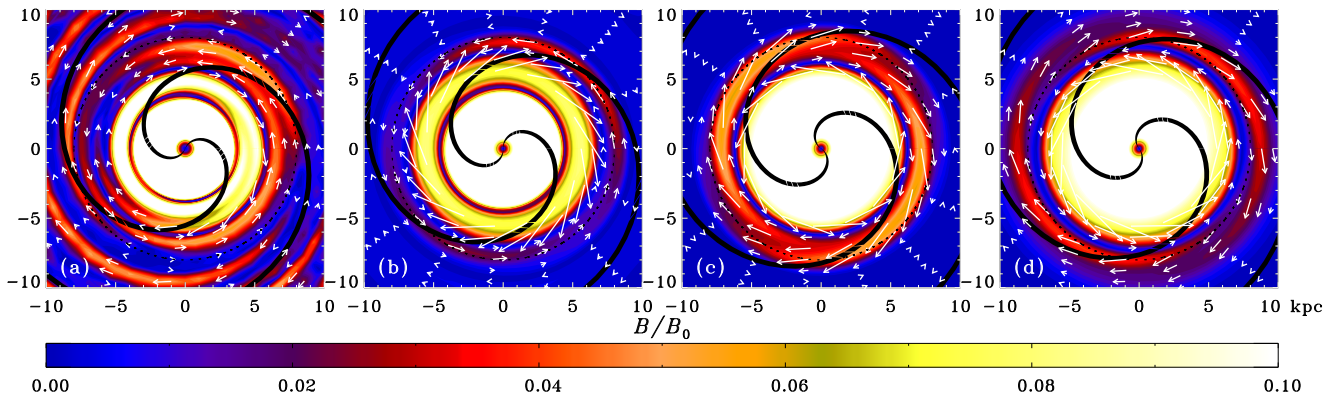


Figure 12. As Fig. 5, but now for Model G (random seed with spiral forcing). The $\tau \rightarrow 0$ case is shown. The peak of α_k is shown as a thick black line, while the corotation radius is marked by the black dotted circle. In addition to reversals, strong deviations from axial symmetry develop near the corotation radius. The morphology of the magnetic field is affected by the outward-moving reversals.

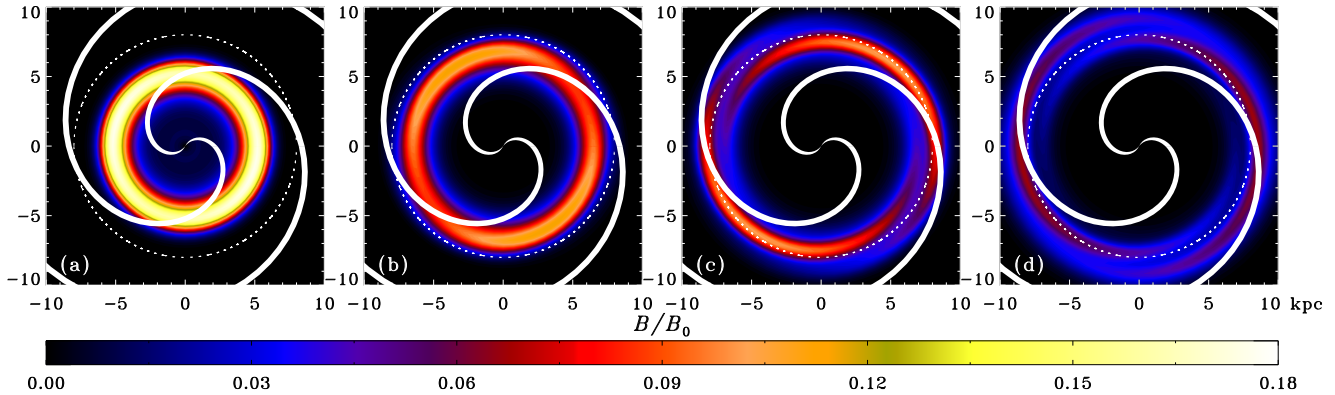


Figure 13. Evolution of the magnitude of the magnetic field in Model H (zero helicity flux, $\bar{U}_z = 0$) and $\tau \rightarrow 0$: (a) $t = 2.2$ Gyr, (b) 3.3 Gyr, (c) 4.4 Gyr, and (d) 5.5 Gyr. The peak of α_k is shown as a thick white line, while the corotation circle is indicated with a white dotted circle. The expanding ring of the mean magnetic field acquires a large $m = 2$ component as it passes by the corotation circle.

$R_U = 0.45$ is close to being optimal. This mechanism for producing magnetic arms located between the material spiral arms was first suggested by Sur et al. (2007).

We find that this mechanism can indeed lead to a non-axisymmetric field which peaks in the inter-arm regions. For the region of parameter space explored, the effect is, however, too weak to be of much consequence, though it might still be important for different parameter values.

5.3.2 Turbulence modulated by the spiral pattern

The characteristic strength of magnetic field at which non-linear dynamo effects become pronounced, B_{eq} , can also be affected by the spiral pattern, e.g., through the variation in the turbulent energy density. We considered a model with B_{eq} enhanced along a spiral in the same way as above for α_k and \bar{U}_z . Since $B_{eq} = (4\pi\rho)^{1/2}u$, and we keep u constant, this is tantamount to modulating ρ . Although an enslaved spiral does result, we find the effect to be too weak to be of much consequence, at least for the parameter space explored.

Other possibilities have been explored in the literature, e.g. the modulation of the turbulent magnetic diffusivity η_t , but a more extensive study of these effects is left for a future work.

5.4 Exploring the parameter space

The purpose of Models G–L is to test the results under reasonable variations of parameters. We have varied the strength of the seed field, the mean vertical velocity \bar{U}_z , the strength and the pitch angle of the spiral pattern via ϵ_α and κ , respectively, and the number of material spiral arms n .

5.4.1 The seed field

In Model G, we use a seed field that is random Gaussian noise. Model G differs from Model C in that the underlying disc is non-axisymmetric. We find reversals to occur in more or less the same locations as in that model. However, as can be seen in Fig. 12 ($\tau \rightarrow 0$ case), a strong quadrupole magnetic field component is now apparent, superimposed

on an axisymmetric pattern with reversals. The morphology of the magnetic spiral arms is significantly affected by the reversals, as the horizontal magnetic field is necessarily zero wherever a reversal occurs (compare, e.g., with Fig. 11a for Model E).

5.4.2 Gas outflow and magnetic helicity flux, \bar{U}_z

The effect of vanishing helicity flux is discussed in Sect. 4.1.1 for the axisymmetric dynamo (Model A). Model H is designed to consider this for non-axisymmetric magnetic fields, and thus differs from Model E only in that it has $\bar{U}_z = 0$. This situation can occur in galaxies after the end of a burst of star formation, when the galactic fountain or wind ceases and the mean-field dynamo action is choked by the magnetic helicity conservation to leave magnetic field decaying, assuming no other flux is important.

As expected, the mean field decays after a period of temporary growth, as shown in Fig. 13 for the nonlinear regime. The expanding annular magnetic structure of Sect. 4.1.1 is prominent, but develops strong deviations from axial symmetry as the ring approaches and then passes through the corotation circle. At late times (not shown), the magnetic ring fades in intensity by about a factor of two in the next 6 Gyr) and becomes more and more axisymmetric as it moves out.

5.4.3 The strength of the spiral pattern, ϵ_α

In Model I, ϵ_α is changed from 0.5, as in Model E, to $\epsilon_\alpha = 1$, so that now $\alpha_k = 0$ between the spiral arms. The saturated solution is illustrated in Fig. 14. As could be expected, this enhances the deviation of the mean magnetic field from axial symmetry, manifested in more pronounced magnetic arms and a larger azimuthal variation in the magnetic pitch angle.

The magnitude of the non-axisymmetric part of the magnetic field mode slightly exceeds the axisymmetric part near $r = r_{\max}$ when $\tau = l_0/u_0$. This produces small regions of positive pitch angle just outside of the corotation, visible in Fig. 14f (darkest regions), where the magnetic lines locally have the shape of a leading spiral. Putting $\tau = l_0/u_0$ also results in a somewhat larger phase shift compared to the

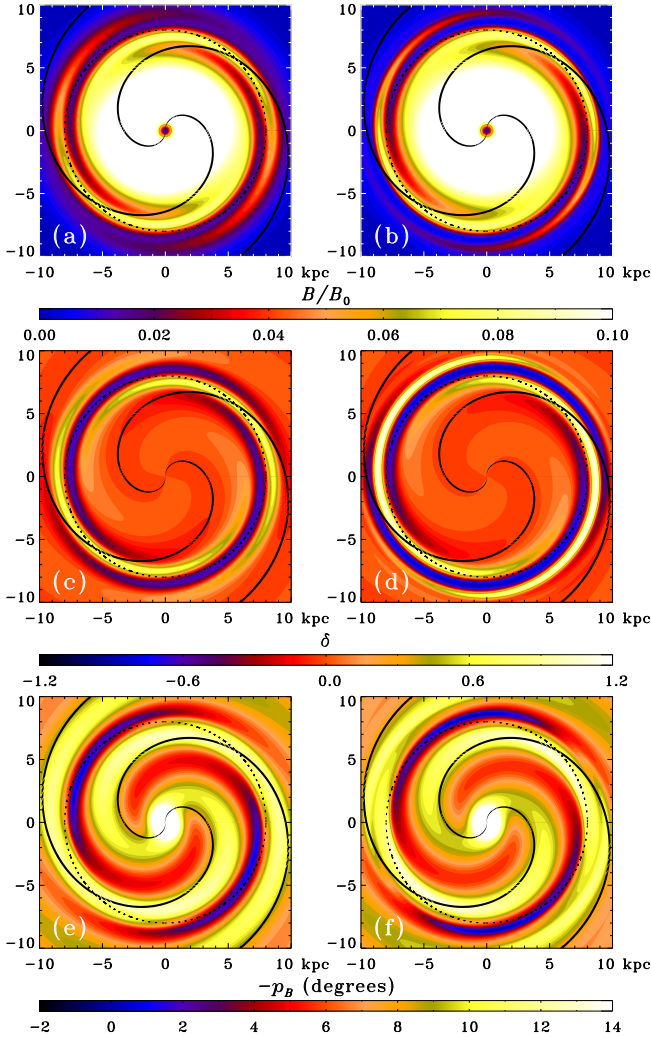


Figure 14. Same as in Fig. 11, but now for Model I ($\epsilon_\alpha = 1$ instead of 0.5), and with the rightmost column of panels omitted. The first column of panels (a, c, e) is for $\tau \rightarrow 0$ while the second column (b, d, f) is for $\tau = l_0/u_0$. The non-axisymmetry of the field is stronger than it is for $\epsilon_\alpha = 0.5$. Note that the very darkest parts of the blue regions in (f) have positive magnetic pitch angle, i.e., magnetic lines in the form of a leading spiral locally.

$\tau = l_0/u_0$ case in Model E. At the radius where the deviations from axial symmetry are the strongest, $r = r_{\max}$, we obtain $\Delta_r(r_{\max}) \simeq \Delta_\phi(r_{\max}) = -36^\circ$ for $\tau = l_0/u_0$, whereas for Model E we had -27° . On the other hand, for $\tau \rightarrow 0$, the phase differences are both equal to $+3^\circ$, the same as in Model E so the overall phase shift is -39° . The trailing part of the magnetic spiral is clearly enhanced when τ is finite.

5.4.4 The pitch angle of the material spirals, κ

In Models J and K we make the α -spiral less tightly wound by reducing the parameter κ . It is evident from Fig. 15 that changing the value of κ from $-20R^{-1}$ ($p_\alpha(r_{\text{cor}}) = -14^\circ$, Model E) to $-8R^{-1}$ ($p_\alpha(r_{\text{cor}}) = -32^\circ$, Model J) does not have any significant qualitative effect on the magnetic field. Even replacing the material spiral with a bar ($\kappa = 0$, Model K) does not lead to a drastic change in the satu-

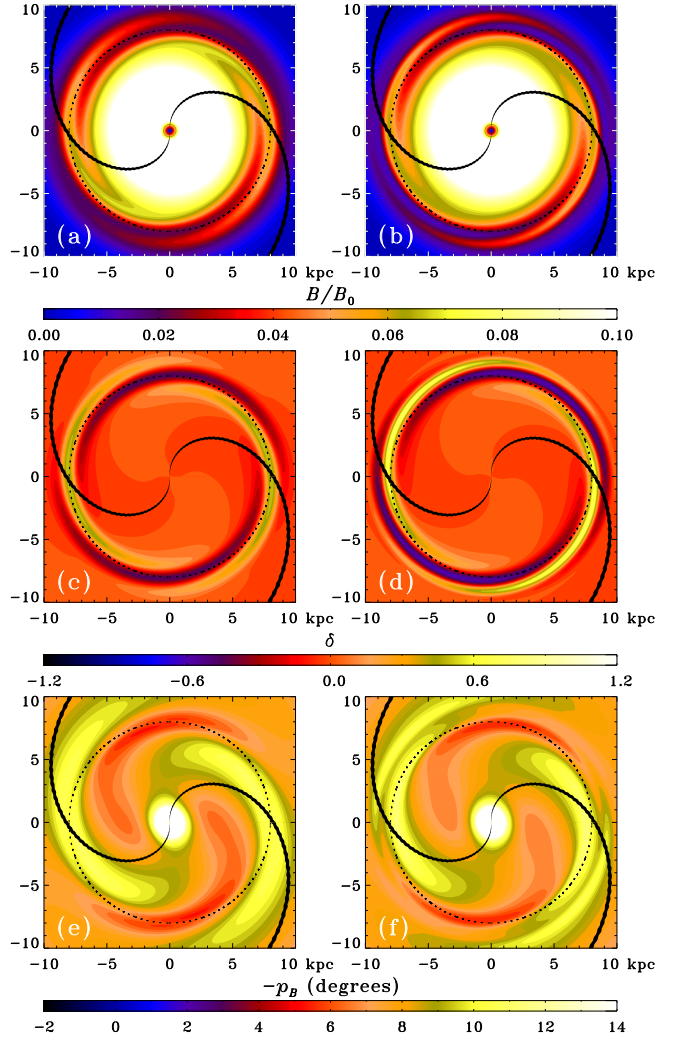


Figure 15. Same as in Fig. 14 but now for Model J ($\epsilon_\alpha = 0.5$ and $\kappa = -8R^{-1}$ instead of $-20R^{-1}$). Magnetic arms are strong in the regions in between the material arms ($\tau \rightarrow 0$ on the left and $\tau = l_0/u_0$ on the right).

rated magnetic field, so that bars also lead to spiral magnetic fields. This happens because of the differential rotation of the gas, which shears out the enhancement of the field due to the bar.

The relative strength of the non-axisymmetric part of the magnetic field is slightly larger in a disc with a more open spiral pattern, which could be expected since the radial magnetic diffusion becomes weaker. An important effect of a more open spiral pattern, visible in Fig. 15a–b, is that magnetic spiral arms are now mostly in between the material arms, although still confined to an annular region around corotation. The values of $\Delta_r(r_{\max})$ and $\Delta_\phi(r_{\max})$ are both -33° for $\tau = l_0/u_0$, and $+3^\circ$ for $\tau \rightarrow 0$. Thus, the finite relaxation time of the mean emf leads to a significantly larger phase shift than in Model E (-36° vs. -27°). The variation of the magnetic pitch angle is strongly modified, because the pitch angle is enhanced where α is large. However, the range of variation in the magnetic pitch angle remains almost unchanged from the case of the more tightly wound spiral pattern of Model E.

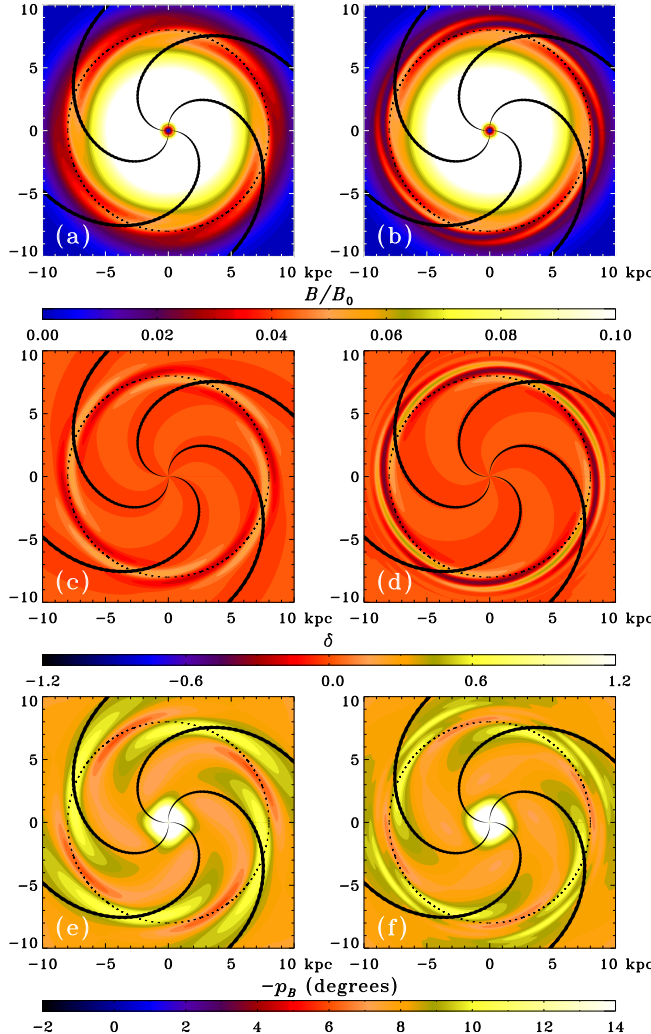


Figure 16. Same as in Fig. 14 but now for Model L ($\epsilon_\alpha = 0.5$ and $n = 4$ instead of 2). Magnetic arms are again strong in the regions in between the material arms. For the $\tau = l_0/u_0$ case (right panels), the magnetic arms are more pronounced than for $\tau \rightarrow 0$, and are mostly trailing the corresponding material arms.

5.4.5 The number of spiral arms, n

We tried various values of n , both odd and even, and found, unsurprisingly, that the number of magnetic arms is equal to the number of material arms. The results of Model L ($n = 4$) are plotted in Fig. 16. The magnetic arms are largely located in between the material arms, especially for $\tau = l_0/u_0$. They are also much stronger and more well-defined in the finite τ case.

6 MAGNETIC RESPONSE TO TRANSIENT SPIRAL PATTERNS

6.1 A rigidly rotating spiral pattern

As galactic spiral patterns may be transient in nature, we now explore, in Model M, how the magnetic field responds to sudden changes in the spiral forcing. The runs are identical to Model B (axisymmetric disc) up until the α -spiral is

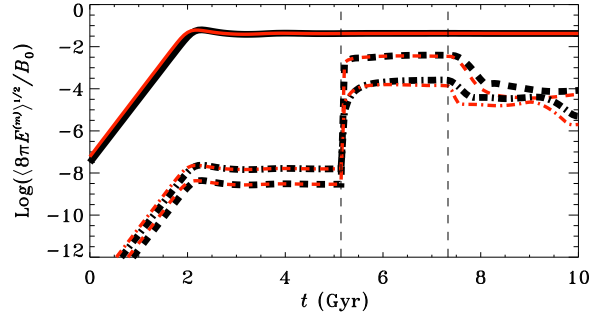


Figure 17. As Fig. 8, but for Model M (transient rigidly rotating spiral). The times at which the α -spiral was turned on and off are indicated by vertical dashed lines.

turned on, at the time $t_{\text{on}} = 5.1$ Gyr, when the dynamo is already in its nonlinear phase. Subsequently, the parameters of the model are identical to those of Model E (standard spiral forcing) up until the time $t_{\text{off}} = 7.3$ Gyr, when the spiral modulation of α is turned off.

The evolution of the magnetic field strength in each Fourier mode, averaged over the area of the disc, is shown in Fig. 17. The $m = 2$ mode, which initially is present solely because of numerical noise, responds rapidly to the onset of the α -spiral, and then behaves almost exactly as in Model E (compare with Fig. 8). In fact, for $\tau = l_0/u_0$, magnetic energy in the $m = 2$ part of the mean field slightly exceeds that in Model E before being reduced to the latter. The timescale of the adjustment of the magnetic field, i.e., the time from the onset of the α -spiral, taken for the $m = 2$ part in Model M to grow up to that in Model E, is as short as $\simeq 0.2$ Gyr. This timescale is shorter than the vertical turbulent diffusion time, but comparable to the dynamo growth time at corotation.

Figure 18 shows characteristic magnetic configurations for $\tau = l_0/u_0$ (the $\tau \rightarrow 0$ case is qualitatively similar so only $\tau = l_0/u_0$ is shown). After a short period of 0.15 Gyr after the onset of the spiral forcing, the deviation from axial symmetry in the magnetic field is strongest somewhat inside of the corotation circle, as can be seen by the location of the peak in amplitude of the dashed envelope in Fig. 18a. This is explained by the dynamo responding more rapidly to sudden changes in the disc at locations where the dynamo number is larger. At $t = t_{\text{on}} + 0.29$ Gyr, the non-axisymmetric component of the field has expanded outward in radius, and has become stronger as compared to the axisymmetric component (panels b and f). This is to be expected since, according to results already discussed, deviations from axisymmetry are most important near the corotation radius. Next, at $t = t_{\text{on}} + 2.2$ Gyr = t_{off} (Fig. 18c and g), the magnetic field has reached nearly the same equilibrium state as in Model E (compare with Figs. 10b and 11b). After the α -spiral has been switched-off, the magnetic arms remain for a rather long time compared with the time it had taken for them to arise. This can be seen in Figs. 18d and h, where we show the field at $t = t_{\text{off}} + 0.37$ Gyr. The energy in the $m = 2$ part declines to a quarter of its value at t_{off} within 0.2 Gyr and 0.3 Gyr, respectively, for $\tau \rightarrow 0$ and $\tau = l_0/u_0$. Therefore, ‘ghost’ magnetic spiral arms remain

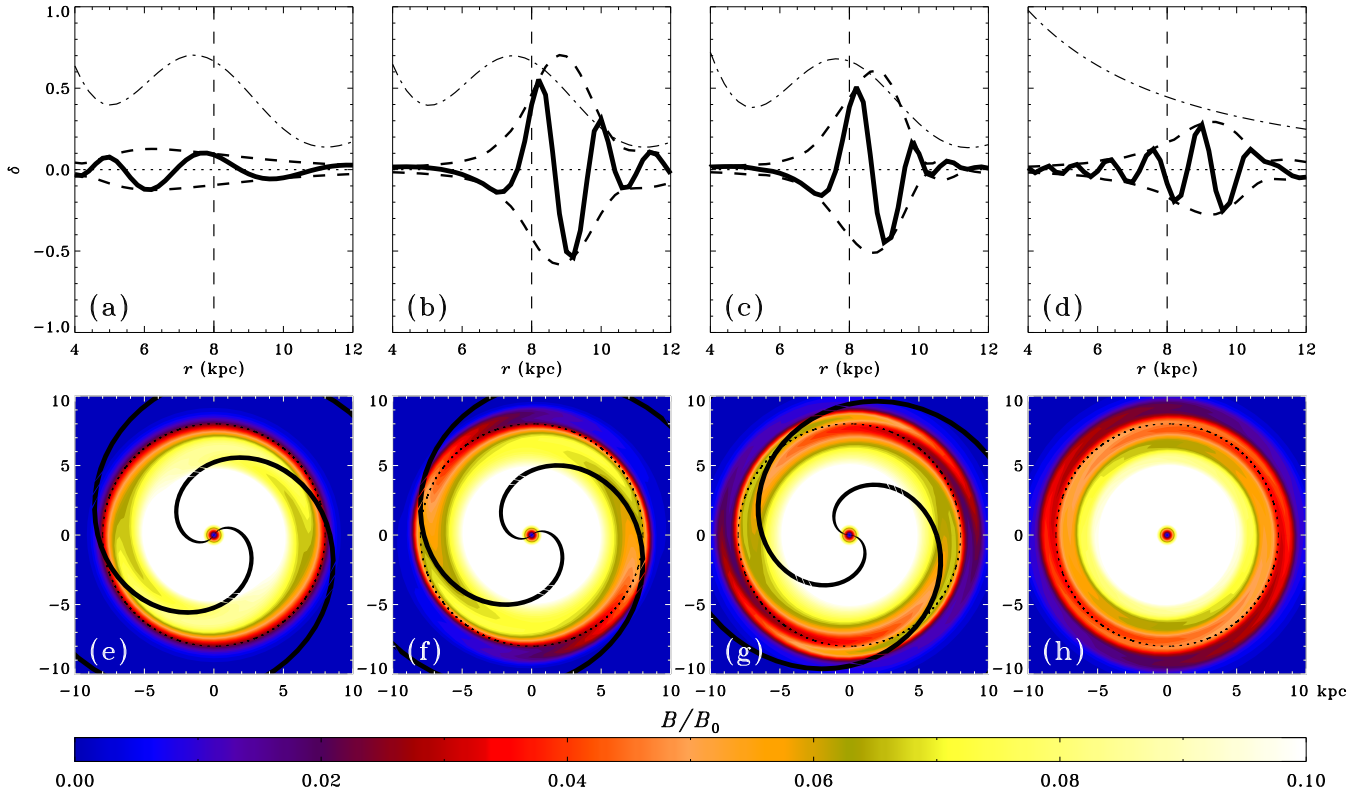


Figure 18. Evolution of the magnetic field under the action of a transient, rigidly rotating α -spiral (Model M) for $\tau = l_0/u_0$. Each column shows the ratio of non-axisymmetric to axisymmetric part of \bar{B}_ϕ , as in Fig. 9 (top) and magnitude of the field as in Fig. 11 (bottom) at the following times after the emergence of the α -spiral: (a, e) 0.15 Gyr, (b, f) 0.29 Gyr, (c, g) 2.2 Gyr, followed by (d, h) 0.37 Gyr after the α -spiral is turned off.

after the demise of the material spiral arms, and survive longer when τ is finite. The extra delay of about 0.1 Gyr due to the finite τ is larger than the delay $\tau \simeq 0.01$ Gyr that might naively be expected.

In summary, (i) a magnetic spiral can arise within a short period of 0.1–0.2 Gyr after the sudden emergence of an α -spiral, (ii) the magnetic spiral may still be obvious a few hundred Myr after its turnoff, especially if τ is large, and (iii) magnetic field responds to the onset of a transient material spiral first inside of the corotation circle, then further outward near the corotation, and then beyond.

6.2 A winding-up spiral pattern

The models described so far had a rigidly rotating spiral with a constant pattern speed. As a consequence, the magnetic spiral arms are localized within a few kpc of the corotation radius. However, magnetic arms, e.g., in the galaxy M51, can be coherent from within about 1 kpc of the galactic centre, out to 10 kpc (Fletcher et al. 2011). Observations of M51 indicate that there does not exist a single pattern speed for the spiral (Shetty et al. 2007), and simulations of that galaxy suggest that the spiral arms wind up with time (Dobbs et al. 2010). Some N-body simulations of disc galaxies find that material spirals have ‘pattern speeds’ decreasing with radius. In some cases, the radial profile of the rotational velocity of the spiral almost matches the rotation curve of the galaxy (Grand et al. 2011). The rigidly rotat-

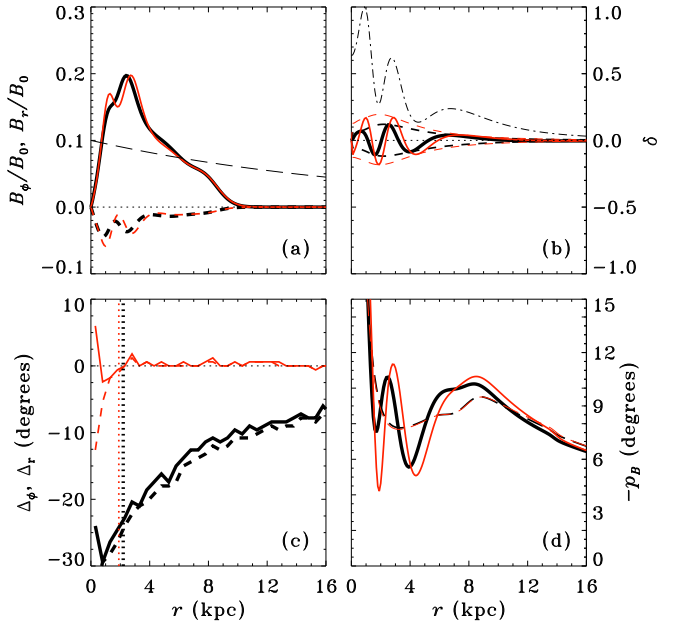


Figure 19. Similar to Fig. 10 (with changes to the plotting ranges), but now for Model N (the α_k spiral winding up with the gas). The figure shows the field at $0.1t_{d,0} \simeq 73$ Myr after the sudden onset of an α_k bar when the dynamo action has already saturated.

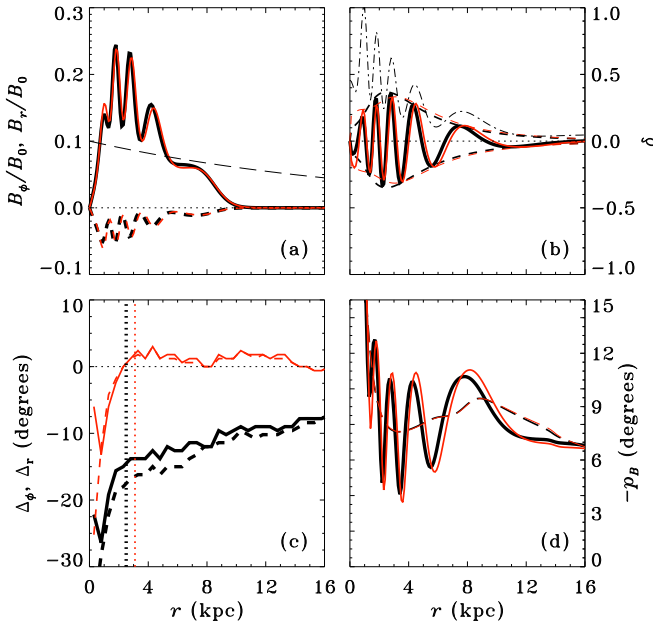


Figure 20. Same as in Fig. 19, but at $0.2t_{d,0} \simeq 146$ Myr after the onset of the α_k bar, (which subsequently winds up into a spiral). The non-axisymmetry is enhanced from the earlier time, and now extends over a larger radial range.

ing spiral model may best characterize some galaxies, while models with spiral winding up with the differential rotation may be more suitable for others – in any case they plausibly represent two extreme cases. A winding-up spiral may also be thought of as the large- N limit of N non-overlapping spiral patterns in the disc.

We have already explored rigidly rotating α -spirals, so we now turn to the case of an α -spiral that winds up with the gas. In this model every radius effectively becomes a corotation radius, so based on our results for a rigidly rotating spiral, we would expect the non-axisymmetric part of the magnetic field to be more extended radially, as seen in some observations. In Model N, the field evolves as in Model B (axisymmetric disc) until the time t_{on} , when we use parameter values $\epsilon_\alpha = 0.5$ and $n = 2$, as in Model E, but now let the spiral wind up starting from the ‘bar’ stage ($\kappa = 0$) at $t = t_{\text{on}} = 6.6$ Gyr, when the $m = 0$ field is already saturated. We find that strong deviations from axial symmetry in the magnetic field develop during the first 150 Myr after t_{on} . In Figs. 19 and 20 we show the properties of the resulting field at two times, $t = t_{\text{on}} + 0.1t_{d,0} = t_{\text{on}} + 73$ Myr and $t_{\text{on}} + 0.2t_{d,0} = t_{\text{on}} + 146$ Myr, respectively.

As can be seen by comparing panels a and b of Fig. 19 ($t = t_{\text{on}} + 73$ Myr) and also by comparing panels a and b of Fig. 20 ($t = t_{\text{on}} + 146$ Myr), the non-axisymmetric and axisymmetric parts of the magnetic field are the strongest at about the same radii, so that the magnetic field is essentially non-axisymmetric. This can also be seen from the colour plots of Fig. 21 ($t = t_{\text{on}} + 73$ Myr) and Fig. 22 ($t = t_{\text{on}} + 146$ Myr). In addition, the magnetic spiral arms are extended throughout the disc over a much larger range of radii than with a rigidly rotating spiral pattern (where the non-axisymmetric field concentrates around the corotation circle).

Figures 19b and 20b show that the radial phase of the field (solid lines) is similar to that of α_k (dash-dotted line), and that the two are well-correlated, demonstrating that the dynamo responds rather quickly to the spiral forcing. From Figs. 19c and 20c, we see that for $\tau \rightarrow 0$ the phase difference between the magnetic and material spiral arms is negligible at radii where the magnetic spiral arms are strong (near where the red solid and dashed lines cross the red dotted vertical line). However, for finite $\tau = l_0/u_0$, the magnetic arms lag the material ones by a large angle, $\Delta_r \simeq \Delta_\phi \simeq -15^\circ$ to -25° over a range of radius of order 10 kpc. The values vary somewhat with radius and with time. This phase shift is strikingly apparent when comparing panels (a) and (e) of Fig. 21 for $\tau \rightarrow 0$ with, respectively, panels (b) and (f) for $\tau = l_0/u_0$. Only in panels (b) and (f) do the yellow-orange regions of high field strength lag the black centers of the α -spiral arms by a significant amount. The same is true in Fig. 22, showing snapshots at $t = t_{\text{on}} + 146$ Myr.

As might be expected, the phase shift is larger for $\tau = 2l_0/u_0$ (-20° to -30°) and even larger for $\tau = 4l_0/u_0$ (-25° to -35°), as can be seen from the third and fourth columns of Figs. 21 and 22. However, as τ is increased, the non-axisymmetric part of the magnetic field tends to weaken, as the spreading of the response of the dynamo in time due to the finite dynamo relaxation time is translated into an effective blurring of the α -spiral in space (the effect is most evident when comparing panels e-h of Fig. 21 or Fig. 22).

We also tried, separately, $\epsilon_\alpha = 1$ and $n = 4$. For $\epsilon_\alpha = 1$, the results are similar to Model N ($\epsilon_\alpha = 0.5$), with a comparable magnitude of the phase shift in the $\tau = l_0/u_0$ case. However, we find magnetic arms that are somewhat stronger and more extended than in Model N, as might be expected from the discussion of Sect. 5.4.3. On the other hand, when n is increased from two to four, we find a four-arm magnetic spiral, as might be expected. Importantly, due to the smaller angle between the material arms, the magnetic arms are located closer to the centres of the inter-arm regions than for the two-arm spiral of Model N (see also Sect. 5.4.5)

This model, which incorporates a spiral pattern that seems to wind up with the differentially rotating gas, along with a dynamo relaxation time $\tau \gtrsim l_0/u_0$, seems to be the most successful, among the models explored in the present work, at explaining the large phase shifts between magnetic and material arms, roughly constant over a large radial range, observed in some galaxies, such as NGC 6946.

7 DISCUSSION AND CONCLUSIONS

We have presented a set of models of the mean-field galactic dynamo action that include: (i) dynamo forcing by stationary and transient spiral structure, (ii) time delay in the response of the mean electromotive force to changes in the mean magnetic field (finite relaxation time τ), and (iii) dynamo nonlinearity based on magnetic helicity balance.

We incorporate into a detailed galactic model a physically and mathematically justifiable dynamo saturation mechanism based on the advection of magnetic helicity by galactic outflows (Shukurov et al. 2006; Sur et al. 2007). Within this framework, we explore the behaviour of the mean magnetic field in both axisymmetric and non-axisymmetric galactic discs. A novel aspect of this paper is

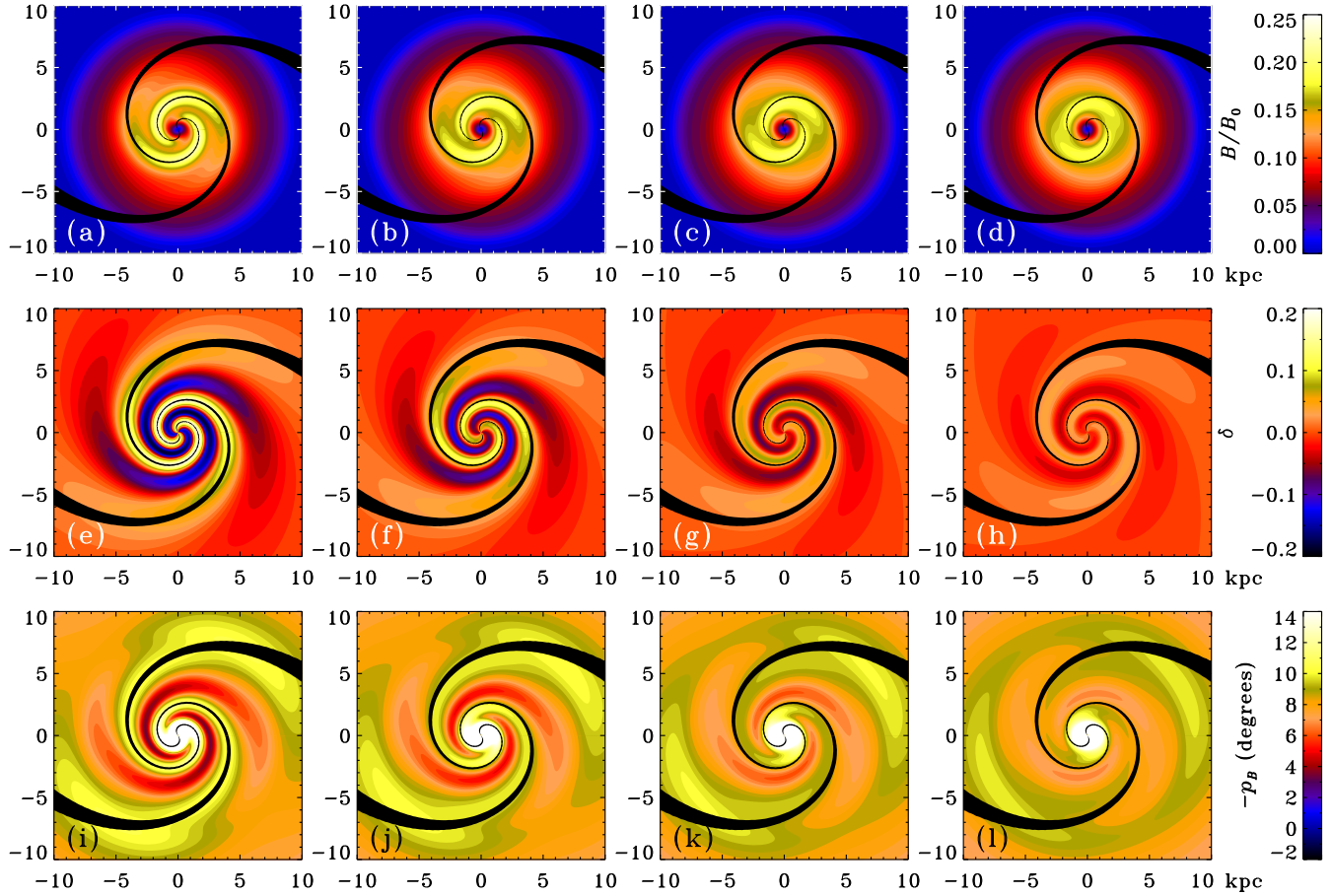


Figure 21. Winding-up spiral of Model N. The figure is similar to Fig. 11. From left to right the columns represent: $\tau \rightarrow 0$, $\tau = l_0/u_0$, $\tau = 2l_0/u_0$, and $\tau = 4l_0/u_0$. All panels are snapshots at $0.1t_{d,0} = 73$ Myr after the sudden onset of the α_k ‘bar’. Increasingly larger phase shifts in the magnetic arms toward the inside of the spiral arms (trailing side) are evident as τ increases.

the introduction of a finite relaxation time into the galactic mean-field theory and a detailed exploration of its effects, particularly on the non-axisymmetric dynamo modes. We discuss how the imprints of the galactic spiral pattern on the morphology of the mean magnetic field are affected by the finite relaxation time of the dynamo. Unlike many earlier studies of galactic dynamos, we approach these problems from the evolutionary viewpoint and consider the magnetic response to both steady and transient spiral patterns, and briefly discuss the diverse ways in which galactic spiral arms can affect the dynamo action.

We have confirmed, in the new framework, earlier results on the evolution of axisymmetric magnetic fields in axisymmetric discs, including the spreading of magnetic fronts along radius and the occurrence of reversals. As expected, the magnetic field is able to spread radially to encompass the whole disc within the galactic lifetime, as long as the magnetic helicity flux is sufficient, but not too large. What is new is that in the absence of any helicity flux, contracting and expanding rings of magnetic field, emanating from the region where the magnitude of the dynamo number is largest, can propagate for several Gyr in the nonlinear regime. This is due to the variation along radius of the time taken for the magnetic field to reach saturation.

The lifetimes of reversals in the galactic disc have been known to be sensitive to the details of the galactic rotation curve, the geometric shape of the gas layer, details of the turbulent energy distribution in the galaxy, etc. We have added another important parameter to this list, the dynamo relaxation time. We also find that such reversals can have non-trivial effects on the morphology of non-axisymmetric magnetic structures in a non-axisymmetric disc. It would be interesting to carry out a more detailed study of magnetic fronts and the possibility of long-lived reversals in the context of the above framework.

We have also shown that it is difficult to maintain non-axisymmetric magnetic structures in an axisymmetric disc, which leaves one little choice but to try to explain such structures as arising from a non-axisymmetric disc. Most of our effort was then directed to the response of the mean magnetic field to the galactic spiral pattern. The focus in this part of our work is the nature of the so-called magnetic arms, spiral-shaped regions of enhanced regular magnetic field (traced by polarised radio emission and, perhaps, Faraday rotation) that are located in between the gaseous and stellar spiral arms in some galaxies (e.g., NGC 6946 and IC 342) but can overlap with or cross the material arms in other galaxies (e.g., M51). We model the effect of the spiral

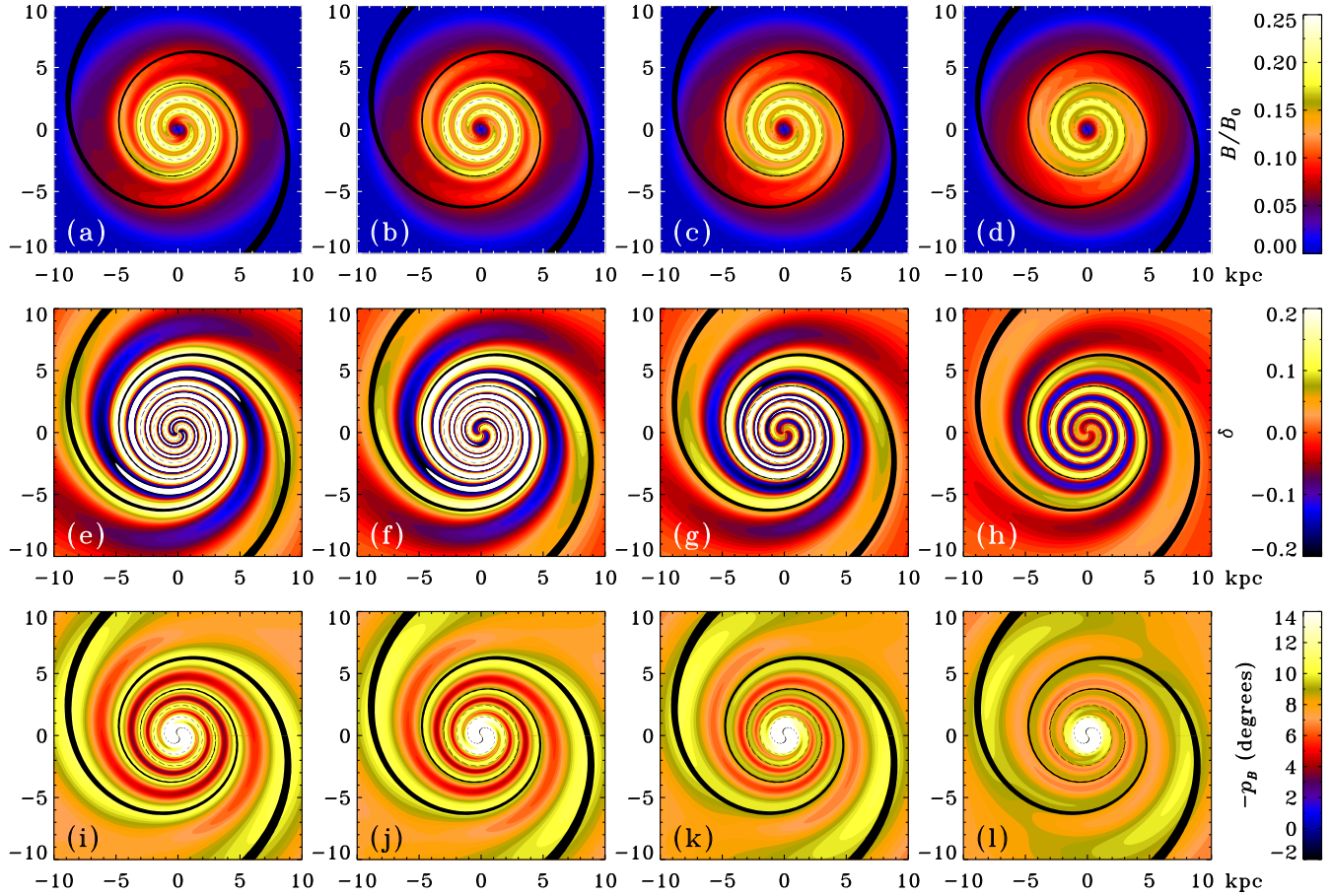


Figure 22. As Fig. 21 but now for $t = t_{\text{on}} + 0.2t_{\text{d},0} = t_{\text{on}} + 146$ Myr. In the middle and bottom rows, the colour in the central region has been saturated to bring out the behaviour at larger radius.

pattern on the dynamo by assuming that the α effect or the galactic/fountain outflow or the equipartition field are enhanced within the spiral arms. A non-axisymmetric α effect, in particular, does lead to strong magnetic arms.

When the dynamo relaxation time $\tau \rightarrow 0$, the magnetic and material arms almost coincide at corotation, as expected from earlier work (MS91; SM93; M96). However, a finite relaxation time causes a significant azimuthal lag between the magnetic and material arms at the radius where the magnetic arms are strongest (near corotation). In this respect, our model can explain a wider range of observations than earlier models. However, we concur with the earlier authors in that the non-axisymmetric parts of the mean magnetic field driven by the spiral pattern are mainly localised around the corotation radius, extending about 4 kpc in radius. The radial extent is, of course, model-dependent and can be larger in regions with weaker rotational velocity shear.

The corotation radius is also approximately where each magnetic arm crosses the corresponding material arm, going from leading (with respect to the direction of the galactic rotation) the material arm inside the corotation circle to trailing it outside the corotation. The primary effect of the finite relaxation time, in the case of a steady, rigidly rotating spiral pattern, is to suppress the leading part of the magnetic

spiral arms and to enhance, and extend azimuthally, the trailing part. Thus, this effect produces a prominent ‘tail’ of large-scale magnetic field in between the material arms. This is even more true when the number of arms is increased from two, to say, four.

The magnetic arms of the spiral galaxy NGC 6946 are ‘interlaced with’ (in between) the material arms (Beck & Høernes 1996; Beck 2007), and have been called ‘phase-shifted images’ of the preceding (in the sense of the rotation) material arms (Frick et al. 2000). Although the implied phase shifts are more constant with radius than in our model, we have obtained a shift of approximately the same magnitude (30° – 40°) and in the right direction. More generally, the shift is of order $\Omega\tau$, where Ω is the pattern angular velocity of the material spiral. Larger values of τ thus lead to larger phase shifts. This is caused by the delay in the α effect of order τ , so that by the time the dynamo has had the chance to respond to the enhancement in α along the material arm, the arm has already rotated by an angle $\approx \Omega\tau$.

Spiral density waves may be transient and we consider how quickly the regular magnetic field can respond to changes in the galactic spiral structure. We find that the response time is small ($\lesssim 0.2$ Gyr). On the other hand, we find that magnetic spiral arms survive for several hundred Myr following the destruction of the material spiral arms

in the dynamo nonlinear regime. Moreover, a finite dynamo relaxation time is found to significantly prolong the life of such lingering magnetic arms. This opens the intriguing possibility of ‘ghost’ magnetic arms, which were produced by material arms that have since disappeared.

Despite the wide range of models considered, our success in reproducing magnetic arms interlaced with the material arms as perfectly as it is believed to happen in NGC 6946 is admittedly limited in models assuming forcing of the dynamo by a steady, rigidly rotating spiral. In addition, this type of spiral forcing leads to magnetic arms concentrated over a smaller range in radius than is observed in many galaxies. Another possibility, rendered more likely by several recent studies (e.g. Dobbs et al. 2010; Sellwood 2011; Quillen et al. 2011), is that the spiral patterns of many galaxies, rather than being rigidly rotating, as is usually assumed in galactic dynamo models, in fact wind up (at least to some extent). This may happen if, for instance, there are interfering two and three-armed spirals rotating at different angular frequencies (A. Quillen, private communication). The two-arm grand design spiral pattern of the galaxy M51 (NGC 5194), thought to be caused by tidal forcing by its neighbour, NGC 5195, is also found to wind up in detailed N-body simulations that are able to accurately reproduce its spiral morphology (Dobbs et al. 2010).

With these recent advances in spiral structure theory in mind, we also investigated the opposite extreme to rigidly rotating patterns: material arms that are wound up by the galactic differential rotation. The nonlinear dynamo responds very quickly to such forcing, and for vanishing dynamo relaxation time the mean magnetic field more or less traces the spiral arms over a large range in radius (as seen in many observations) and winds up with them. On the other hand, for finite dynamo relaxation time there is a large azimuthal lag of each magnetic spiral arm compared to the corresponding material arm over a large range in radius. Magnetic arms trail the material arms by 15° – 25° (for $\tau = l_0/u_0$), varying somewhat with time and radius over the disc. This shift is of order $\omega\tau$, where ω is the angular velocity of the gas, and we have shown that larger, but still plausible, values of τ , lead to even larger phase shifts. Increasing the number of spiral arms also causes the (equal number of) magnetic arms to be located closer to the centres of the inter-arm regions, so that they may be described as interlaced with the material arms. Therefore, allowing for the possibility of the spiral winding up can drastically improve agreement with observations of the regular magnetic fields in some galaxies, but with the trade-off that the magnetic arms (that in this model, either trace or interlace the material arms) are almost as short-lived as the spiral patterns that presumably generate them.

In summary, we have incorporated into galactic dynamo theory several well-studied physical effects not previously considered, namely (i) non-locality in time and (ii) forcing by both spiral arms which steadily rotate and those which wind up due to differential rotation. This allows several observed features of magnetic arms to be more naturally reproduced. Particularly interesting are the models we have presented in which magnetic arms extend over a large range of radii and either trace material arms over several kpc, or else are phase-shifted images of material arms, trailing them in the sense of the galactic rotation. It would be interesting and

important to test these ideas by applying them to specific galaxies, for which the rotation curve, velocity dispersion, spiral structure, etc., can be constrained by existing data from observation and simulation.

ACKNOWLEDGMENTS

We are grateful to Sharanya Sur for sharing with us his preliminary results on incorporating MTA into the galactic mean-field dynamo equations and for many useful discussions. LC wishes to thank Axel Brandenburg for initial help with the simulations and for generously sharing his many routines, as well as for useful discussions. We also thank Nishant Singh for reading a draft of the manuscript and providing valuable suggestions. AS is grateful to IUCAA for financial support. KS acknowledges partial support from NSF Grant PHY-0903797 while at the University of Rochester. KS thanks Eric Blackman at Rochester for warm hospitality and both him and Alice Quillen for interesting discussions.

APPENDIX A: A MORE GENERAL FORM OF THE BASIC EQUATIONS

A1 The telegraph equation

Having defined

$$\mathcal{F} \equiv \nabla \times \mathcal{E},$$

and assuming that η , η_t , τ and c_τ are constants, the cylindrical polar components of Eq. (3) can be written as

$$\begin{aligned} \frac{\partial \bar{B}_r}{\partial t} = & \frac{1}{r} \frac{\partial}{\partial \phi} (\bar{U}_r \bar{B}_\phi - \bar{U}_\phi \bar{B}_r) - \frac{\partial}{\partial z} (\bar{U}_z \bar{B}_r - \bar{U}_r \bar{B}_z) \\ & + \eta \left\{ \frac{\partial}{\partial r} \left[\frac{1}{r} \frac{\partial}{\partial r} (r \bar{B}_r) \right] + \frac{1}{r^2} \frac{\partial^2 \bar{B}_r}{\partial \phi^2} + \frac{\partial^2 \bar{B}_r}{\partial z^2} - \frac{2}{r^2} \frac{\partial \bar{B}_\phi}{\partial \phi} \right\} \\ & + \mathcal{F}_r, \end{aligned} \quad (A1)$$

$$\begin{aligned} \frac{\partial \bar{B}_\phi}{\partial t} = & \frac{\partial}{\partial z} (\bar{U}_\phi \bar{B}_z - \bar{U}_z \bar{B}_\phi) - \frac{\partial}{\partial r} (\bar{U}_r \bar{B}_\phi - \bar{U}_\phi \bar{B}_r) \\ & + \eta \left\{ \frac{\partial}{\partial r} \left[\frac{1}{r} \frac{\partial}{\partial r} (r \bar{B}_\phi) \right] + \frac{1}{r^2} \frac{\partial^2 \bar{B}_\phi}{\partial \phi^2} + \frac{\partial^2 \bar{B}_\phi}{\partial z^2} + \frac{2}{r^2} \frac{\partial \bar{B}_r}{\partial \phi} \right\} \\ & + \mathcal{F}_\phi, \end{aligned} \quad (A2)$$

$$\begin{aligned} \frac{\partial \bar{B}_z}{\partial t} = & \frac{1}{r} \frac{\partial}{\partial r} [r(\bar{U}_z \bar{B}_r - \bar{U}_r \bar{B}_z)] - \frac{1}{r} \frac{\partial}{\partial \phi} (\bar{U}_\phi \bar{B}_z - \bar{U}_z \bar{B}_\phi) \\ & + \eta \left\{ \frac{1}{r} \frac{\partial}{\partial r} \left(r \frac{\partial \bar{B}_z}{\partial r} \right) + \frac{1}{r^2} \frac{\partial^2 \bar{B}_z}{\partial \phi^2} + \frac{\partial^2 \bar{B}_z}{\partial z^2} \right\} + \mathcal{F}_z. \end{aligned} \quad (A3)$$

Taking the curl of both sides of Eq. (9), we get

$$\begin{aligned} \tau \frac{\partial \mathcal{F}_r}{\partial t} = & c_\tau \left\{ \frac{1}{r} \frac{\partial}{\partial \phi} (\alpha \bar{B}_z) - \frac{\partial}{\partial z} (\alpha \bar{B}_\phi) \right\} + c_\tau \eta_t \left\{ \frac{\partial}{\partial r} \left[\frac{1}{r} \frac{\partial}{\partial r} (r \bar{B}_r) \right] \right. \\ & \left. + \frac{1}{r^2} \frac{\partial^2 \bar{B}_r}{\partial \phi^2} + \frac{\partial^2 \bar{B}_r}{\partial z^2} - \frac{2}{r^2} \frac{\partial \bar{B}_\phi}{\partial \phi} \right\} - \mathcal{F}_r, \end{aligned} \quad (A4)$$

$$\begin{aligned} \tau \frac{\partial \mathcal{F}_\phi}{\partial t} = & c_\tau \left[\frac{\partial}{\partial z} (\alpha \bar{B}_r) - \frac{\partial}{\partial r} (\alpha \bar{B}_z) \right] + c_\tau \eta_t \left\{ \frac{\partial}{\partial r} \left[\frac{1}{r} \frac{\partial}{\partial r} (r \bar{B}_\phi) \right] \right. \\ & \left. + \frac{1}{r^2} \frac{\partial^2 \bar{B}_\phi}{\partial \phi^2} + \frac{\partial^2 \bar{B}_\phi}{\partial z^2} + \frac{2}{r^2} \frac{\partial \bar{B}_r}{\partial \phi} \right\} - \mathcal{F}_\phi, \end{aligned} \quad (\text{A5})$$

$$\begin{aligned} \tau \frac{\partial \mathcal{F}_z}{\partial t} = & c_\tau \left[\frac{1}{r} \frac{\partial}{\partial r} (r \alpha \bar{B}_\phi) - \frac{1}{r} \frac{\partial}{\partial \phi} (\alpha \bar{B}_r) \right] \\ & + c_\tau \eta_t \left[\frac{1}{r} \frac{\partial}{\partial r} \left(r \frac{\partial \bar{B}_z}{\partial r} \right) + \frac{1}{r^2} \frac{\partial^2 \bar{B}_z}{\partial \phi^2} + \frac{\partial^2 \bar{B}_z}{\partial z^2} \right] - \mathcal{F}_z. \end{aligned} \quad (\text{A6})$$

A2 Dynamical quenching by advective flux

Assuming that $\alpha = \alpha_k + \alpha_m$, that is, the α effect can be separated into kinetic and magnetic contributions, we have (Shukurov et al. 2006; Subramanian & Brandenburg 2006)

$$\frac{\partial \alpha_m}{\partial t} = -\frac{2\eta_t}{l^2} \left(\frac{\mathcal{E} \cdot \bar{\mathbf{B}}}{B_{\text{eq}}^2} + \frac{\alpha_m}{\mathcal{R}_m} \right) - \nabla \cdot (\alpha_m \bar{\mathbf{U}}), \quad (\text{A7})$$

where $B_{\text{eq}}^2 = 4\pi\rho u^2$ is the equipartition field strength and $\mathcal{R}_m = \eta_{t,0}/\eta$ is the magnetic Reynolds number. To evaluate the term containing \mathcal{E} , we need the evolution equations for its components. From Eq. (9), we find

$$\tau \frac{\partial \mathcal{E}_r}{\partial t} = c_\tau \alpha \bar{B}_r - c_\tau \eta_t \left(\frac{1}{r} \frac{\partial \bar{B}_z}{\partial \phi} - \frac{\partial \bar{B}_\phi}{\partial z} \right) - \mathcal{E}_r, \quad (\text{A8})$$

$$\tau \frac{\partial \mathcal{E}_\phi}{\partial t} = c_\tau \alpha \bar{B}_\phi - c_\tau \eta_t \left(\frac{\partial \bar{B}_r}{\partial z} - \frac{\partial \bar{B}_z}{\partial r} \right) - \mathcal{E}_\phi, \quad (\text{A9})$$

$$\tau \frac{\partial \mathcal{E}_z}{\partial t} = c_\tau \alpha \bar{B}_z - c_\tau \eta_t \left[\frac{1}{r} \frac{\partial}{\partial r} (r \bar{B}_\phi) - \frac{1}{r} \frac{\partial \bar{B}_r}{\partial \phi} \right] - \mathcal{E}_z. \quad (\text{A10})$$

The evolution equations for \mathcal{E} are redundant given those for \mathcal{F} , since the latter could be obtained by taking the curl of the former. However, we find it convenient to solve separately for \mathcal{E} and \mathcal{F} (see Sect. 3.1).

APPENDIX B: THE NO- z APPROXIMATION

B1 Vertical diffusion

Under the no- z approximation, the second derivatives with respect to z can be approximated as $\partial^2 \bar{B}_i / \partial z^2 \simeq -\pi^2 \bar{B}_i / 4h^2$ (where $i = r, \phi$), which gives the correct sign of the diffusion term. This approximation can be derived from the one-dimensional eigenfunctions obtained from the perturbation theory (Sur et al. 2007; Shukurov & Sokoloff 2008).

B2 The α effect

When applying the no- z approximation to the terms $\partial(\alpha \bar{B}_i) / \partial z$ in Eqs. (A4) and (A5), one must be careful about the sign. The sign must be chosen so that the α effect can contribute to a positive dynamo growth rate. This logic leads to the adoption of the approximations

$$-\frac{\partial}{\partial z} (\alpha \bar{B}_\phi) \approx -\frac{|\alpha| \bar{B}_\phi}{h}, \quad \frac{\partial}{\partial z} (\alpha \bar{B}_r) \approx \frac{|\alpha| \bar{B}_r}{h}.$$

The second of these is only relevant when the α^2 effect is taken into consideration.

Furthermore, Phillips (2001) has shown that the no- z approximation can be made more accurate with the additional numerical factor $2/\pi$, at least for the $\alpha\omega$ dynamo. As a matter of symmetry, we include the same numerical factor in front of both α terms, so that we may write

$$-\frac{\partial}{\partial z} (\alpha \bar{B}_\phi) \approx -\frac{2|\alpha| \bar{B}_\phi}{\pi h}, \quad \frac{\partial}{\partial z} (\alpha \bar{B}_r) \approx \frac{2|\alpha| \bar{B}_r}{\pi h}. \quad (\text{B1})$$

It may be asked whether extending the no- z approximation to include the α term in the evolution equation for \bar{B}_ϕ (through Eq. A5), as we have done here for the first time, actually helps to improve the accuracy of the solution. To answer this, we compared the solutions obtained using simple two-dimensional (in $r-z$) $\alpha\omega$ and $\alpha^2\omega$ galactic dynamo model with those obtained from the corresponding one-dimensional (in r , with no- z) models. Interestingly, we found significantly better agreement between the 1D and 2D solutions when the α^2 effect was included in both models than when it was left out.

B3 Vertical advection

The terms $-\bar{\mathbf{B}} \nabla \cdot \bar{\mathbf{U}}$ (divergence) and $-\bar{\mathbf{U}} \cdot \nabla \bar{\mathbf{B}}$ (advection) are approximated as

$$\frac{\partial \bar{B}_i}{\partial t} = \dots - \frac{\partial \bar{U}_z}{\partial z} \bar{B}_i - \bar{U}_z \frac{\partial \bar{B}_i}{\partial z} \simeq \dots - \frac{\bar{U}_z \bar{B}_i}{h}. \quad (\text{B2})$$

For $-\partial(\alpha_m \bar{U}_z) / \partial z$ in (A7), we have

$$\frac{\partial \alpha_m}{\partial t} = \dots - \frac{\alpha_m \bar{U}_z}{h}. \quad (\text{B3})$$

B4 Approximation for $\mathcal{E} \cdot \bar{\mathbf{B}}$

For $\tau \rightarrow 0$, we have

$$\mathcal{E} \cdot \bar{\mathbf{B}} = c_\tau \alpha (\bar{B}_r^2 + \bar{B}_\phi^2) + c_\tau \eta_t \left(\bar{B}_r \frac{\partial \bar{B}_\phi}{\partial z} - \bar{B}_\phi \frac{\partial \bar{B}_r}{\partial z} \right), \quad (\text{B4})$$

and the second bracketed term arising from the mean current helicity vanishes in the no- z approximation. Therefore, a more precise method must be used to estimate this term. With this in mind, Sur et al. (2007) substituted the one-dimensional perturbation solution of the dynamo equations,

$$\bar{B}_r = R_\alpha C_0 \left(\cos \frac{\pi z}{2h} + \frac{3}{4\pi} \sqrt{\frac{-D}{\pi}} \cos \frac{3\pi z}{2h} \right), \quad (\text{B5})$$

$$\bar{B}_\phi = -2C_0 \sqrt{\frac{-D}{\pi}} \cos \frac{\pi z}{2h}, \quad (\text{B6})$$

and its derivatives with respect to z into Eq. (B4). The resulting expression for $\mathcal{E} \cdot \bar{\mathbf{B}}$ was then averaged over $0 \leq z \leq h$. In this way they obtained a non-zero estimate for $c_\tau \eta_t (\bar{B}_r \partial \bar{B}_\phi / \partial z - \bar{B}_\phi \partial \bar{B}_r / \partial z)$, which stems from the term of order $\sqrt{-D}$ in Eq. (B5).

In the general case of finite τ , the correction must come in the evolution equations (A8) and (A9) for \mathcal{E}_r and \mathcal{E}_ϕ . Averaging Eqs. (B5) and (B6) and also their z -derivatives over $0 \leq z \leq h$, we find

$$\frac{\partial \bar{B}_r}{\partial z} \simeq -\frac{\pi}{2h} \left(1 + \frac{3\sqrt{-D}}{4\pi^{3/2}} \right) \bar{B}_r, \quad (\text{B7})$$

$$\frac{\partial \overline{B}_\phi}{\partial z} = -\frac{\pi}{2h} \overline{B}_\phi. \quad (B8)$$

These expressions are used in Eqs. (A8) and (A9) for calculating $\mathbf{\mathcal{E}} \cdot \overline{\mathbf{B}}$ in Eq. (A7).

Substituting expressions (B7) and (B8) into Eq. (B4), we find for the $\tau \rightarrow 0$ limit,

$$\mathbf{\mathcal{E}} \cdot \overline{\mathbf{B}} \simeq c_\tau \alpha (\overline{B}_r^2 + \overline{B}_\phi^2) + c_\tau \eta_t \frac{3\sqrt{-D}}{8\pi^{1/2} h} \overline{B}_r \overline{B}_\phi. \quad (B9)$$

The term involving η_t used here is smaller by a factor π than that of Sur et al. (2007) since we have taken the scalar product of the z -averages of $\mathbf{\mathcal{E}}$ and $\overline{\mathbf{B}}$, whereas those authors used the average of the scalar product. This difference does not appear to be important.

REFERENCES

Acharova I. A., Mishurov Y. N., Rasulova M. R., 2011, MNRAS, 415, L11

Baryshnikova I., Shukurov A., Ruzmaikin A., Sokoloff D. D., 1987, A&A, 177, 27

Beck R., 2007, A&A, 470, 539

—, 2012, SSRv, 166, 215

Beck R., Hoernes P., 1996, Nat, 379, 47

Blackman E. G., Field G. B., 2000, ApJ, 534, 984

—, 2002, Physical Review Letters, 89, 265007

Brandenburg A., 2003, Computational aspects of astrophysical MHD and turbulence, Taylor & Francis, London and New York, p. 269

Brandenburg A., Subramanian K., 2005a, PhR, 417, 1

—, 2005b, A&A, 439, 835

—, 2007, Astronomische Nachrichten, 328, 507

Bykov A., Popov V., Shukurov A., Sokoloff D., 1997, MNRAS, 292, 1

Courant R., Hilbert D., 1989, Methods of mathematical physics. John Wiley & Sons, New York

Dobbs C. L., 2011, Memorie della Societa Astronomica Italiana Supplementi, 18, 109

Dobbs C. L., Theis C., Pringle J. E., Bate M. R., 2010, MNRAS, 403, 625

Fletcher A., 2010, in Astronomical Society of the Pacific Conference Series, Vol. 438, Astronomical Society of the Pacific Conference Series, Kothes R., Landecker T. L., Willis A. G., eds., p. 197

Fletcher A., Beck R., Shukurov A., Berkhuijsen E. M., Horellou C., 2011, MNRAS, 412, 2396

Frick P., Beck R., Shukurov A., Sokoloff D., Ehle M., Kamphuis J., 2000, MNRAS, 318, 925

Gerhard O., 2011, Memorie della Societa Astronomica Italiana Supplementi, 18, 185

Grand R. J. J., Kawata D., Cropper M., 2011, ArXiv e-prints

Gruzinov A. V., Diamond P. H., 1994, Physical Review Letters, 72, 1651

Hughes D. W., Proctor M. R. E., 2010, Physical Review Letters, 104, 024503

Kawata D., Grand R., Cropper M., 2011, ArXiv e-prints

Khoperskov A. V., Eremim M. A., Khoperskov S. A., Butenko M. A., Morozov A. G., 2011, ArXiv e-prints

Kleeorin N., Mond M., Rogachevskii I., 1996, A&A, 307, 293

Kleeorin N., Moss D., Rogachevskii I., Sokoloff D., 2000, A&A, 361, L5

—, 2002, A&A, 387, 453

Kleeorin N., Ruzmaikin A. A., 1982, Magnetohydrodynamics, 18, 116

Krasheninnikova I., Shukurov A., Ruzmaikin A., Sokoloff D., 1989, A&A, 213, 19

Krause F., Raedler K.-H., 1980, Mean-field magnetohydrodynamics and dynamo theory. Pergamon Press, Oxford

Mestel L., Subramanian K., 1991, MNRAS, 248, 677

Moffatt H. K., 1978, Magnetic field generation in electrically conducting fluids. Cambridge University Press, Cambridge, England

Moss D., 1995, MNRAS, 275, 191

—, 1996, A&A, 308, 381

—, 1998, MNRAS, 297, 860

Moss D., Shukurov A., Sokoloff D., 1998, Geophysical and Astrophysical Fluid Dynamics, 89, 285

Moss D., Shukurov A., Sokoloff D., Beck R., Fletcher A., 2001, A&A, 380, 55

Moss D., Stepanov R., Arshakian T. G., Beck R., Krause M., Sokoloff D., 2012, A&A, 537, A68

Phillips A., 2001, Geophysical and Astrophysical Fluid Dynamics, 94, 135

Poezd A., Shukurov A., Sokoloff D., 1993, MNRAS, 264, 285

Pouquet A., Frisch U., Leorat J., 1976, Journal of Fluid Mechanics, 77, 321

Quillen A. C., Dougherty J., Bagley M. B., Minchev I., Comparetta J., 2011, MNRAS, 417, 762

Rädler K.-H., Kleeorin N., Rogachevskii I., 2003, Geophysical and Astrophysical Fluid Dynamics, 97, 249

Raedler K.-H., 1986, Astronomische Nachrichten, 307, 89

Rheinhardt M., Brandenburg A., 2012, Astronomische Nachrichten, 333, 71

Rogachevskii I., Kleeorin N., 2000, PhRvE, 61, 5202

Rohde R., Beck R., Elstner D., 1999, A&A, 350, 423

Roškar R., Debattista V. P., Quinn T. R., Wadsley J., 2011, ArXiv e-prints

Ruzmaikin A. A., Shukurov A. M., Sokoloff D. D., 1988, Magnetic fields of galaxies. Kluwer, Dordrecht

Sellwood J. A., 2011, MNRAS, 410, 1637

Shetty R., Vogel S. N., Ostriker E. C., Teuben P. J., 2007, ApJ, 665, 1138

Shukurov A., 2004, ArXiv e-prints

Shukurov A., 2005, in Lecture Notes in Physics, Berlin Springer Verlag, Vol. 664, Cosmic Magnetic Fields, Wielebinski R., Beck R., eds., p. 113

Shukurov A., Sokoloff D., 2008, in Les Houches, Vol. 88, Dynamos, Cardin P., Cugliandolo L. F., eds., Elsevier, pp. 251–299

Shukurov A., Sokoloff D., Subramanian K., Brandenburg A., 2006, A&A, 448, L33

Smith A., 2012, PhD thesis, School of Mathematics and Statistics, Newcastle University, Newcastle Upon Tyne

Smith A., Fletcher A., Shukurov A., 2012, In preparation

Subramanian K., Brandenburg A., 2006, ApJ, 648, L71

Subramanian K., Mestel L., 1993, MNRAS, 265, 649

Sur S., Shukurov A., Subramanian K., 2007, MNRAS, 377, 874

Van Eck C. L., Brown J. C., Stil J. M., Rae K., Mao S. A., Gaensler B. M., Shukurov A., Taylor A. R., Havercorn

M., Kronberg P. P., McClure-Griffiths N. M., 2011, ApJ,
728, 97

Vishniac E. T., Cho J., 2001, ApJ, 550, 752

Wada K., Baba J., Saitoh T. R., 2011, ArXiv e-prints